

Imperial College London

SHELL ECO-MARATHON: CHASSIS AND STEERING



FINAL REPORT

Group 26

June 2020

ME3 – Design Make and Test

TEAM MEMBERS

Asad Raja

Carlos Firgau

Jessica Eichel

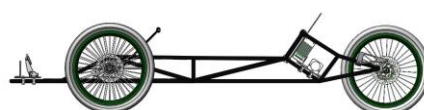
Rahman Al-Shabazz

SUPERVISOR

Alexis Ihracska

CO-SUPERVISOR

Marc Masen



EXECUTIVE SUMMARY

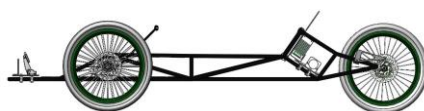
The aim of this project was to design, make and test the chassis and steering system of Imperial Racing Green's entry to the Prototype Class of the 2020 Shell Eco-marathon. Imperial Racing Green is an interdisciplinary society at Imperial College London that allows students to develop vehicles for established racing competitions. Shell Eco-marathon is one of these competitions, in which vehicles compete to complete a set number of laps with the least energy consumption. The vehicle produced would have to satisfy Shell Eco-marathon race regulations whilst improving upon Imperial Racing Green's previous entry, in particular by reducing upon its weight to improve efficiency.



Figure 1 - final solution CAD render

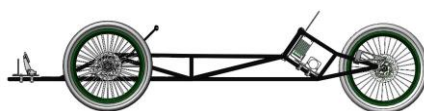
The project was split into three main areas of focus: the chassis structure, the powertrain interface and the steering system. Design development led to a spaceframe chassis made from carbon fibre with key target dimensions of a 500 mm track width and 1550 mm wheelbase. Prototyping was used to develop and optimise the carbon fibre tube wet lay-up joining method, and 3-point bending tests were conducted to obtain Young's Modulus and yield strength values for both a joint section and a plain tube, that were used in analysis to verify the acceptability of stresses and deflections in the chassis. The steering system's efficiency was successfully optimised with an Ackermann geometry configuration that was designed around target kingpin inclination and caster angles of 12° and 4° respectively, whilst offering adjustable toe and camber angles that allowed the target of 0° for each to be met for any driver. The final product, shown in Figure 1, was a chassis and steering system that was lightweight, ergonomic, was successfully manufactured on-site and could fit in the shell of the previous entry whilst allowing all powertrain components to be mounted. Its total weight of 13.85 kg represents a 23% reduction compared to the previous entry. This exceeds the 10% target reduction.

The final testing stage was underway when the project was cut short due to the lockdown, meaning the remaining performance testing and further regulation compliance testing that had been planned could not be conducted. To make up for this, an alternative work package was agreed upon with the Project Supervisor that would include spaceframe deflection hand calculations using energy methods, a spaceframe finite element analysis and failure mode considerations and mitigations. The sections of this report that pertain to this alternative work package have been denoted by 'AWP'.

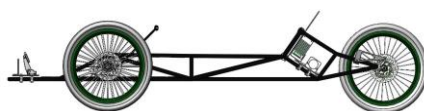


CONTENTS

Executive Summary	2
Contents	3
Introduction and Project Background	5
Competition Structure.....	5
Project Aims and Objectives.....	5
Shell Eco-marathon Team	7
Chassis Design	8
Design Development	8
Wheelbase and Track Width	8
Different Types (monocoque, spaceframe, ladder, backbone)	11
Materials Selection.....	12
Materials Selection of Spaceframe Chassis	12
Square vs Round Profile.....	13
Connection Method for Spaceframe	14
Panel Materials Selection	15
Spaceframe Joint Material Corroboration	15
Risk Assessment	16
Prototype Testing.....	17
Wet Layup Test of Joints	17
3 Point Bending Test: test joint vs plain tube	17
Final Design Process	19
Powertrain Interface	19
Anthropometrics and Ergonomics.....	23
Incorporation into the Design	24
Final Chassis Design.....	25
Validation of Design	25
Modes of Deflection for Automotive Chassis	25
Spaceframe Deflections and Stresses.....	26
Finite Element Analysis Corroboration of Chassis Design (AWP).....	33
Manufacturing of Spaceframe.....	36
Chassis Assembly.....	36
Final Layup Process	36
Powertrain Interfaces	38
Motor Mounting.....	38



Axle Mount Component	39
Steering Design.....	42
Steering Geometry and Variable Angles	42
Introduction to Adjustable Steering Angles	42
Kingpin Inclination	43
Caster	43
Steering Angles Selection	44
Steering Linkages Geometry.....	46
Interface Between Steering Input and Front Wheels	46
Driver Control and Actuation Method.....	48
Steering Design Process	49
Bearing Selection and Design Considerations	49
Provisional Steering Assembly Design	53
Wheel Spindle and 'L' Bracket Assemblies	53
Brake Caliper Mounting Arm	55
Steering Column	57
Stress Analysis of Steering Column Assembly.....	59
Mounting of Steering System to Chassis	64
Final Steering Assembly Design	65
Manufacturing and Assembly of Steering System	66
Manufacturing Methods of Components	66
Manufacturing Progress	67
Mounting of Steering Assembly onto the Chassis	68
Testing and Modifications	70
Components Inspection	70
Ergonomics Testing	71
Regulation Compliance.....	72
Additional Planned Testing.....	73
Budget.....	75
Discussion and Conclusions.....	76
Potential Component Failure and Mitigation (AWP)	76
Conclusions	77
Individual Critiques	78
References	80



INTRODUCTION AND PROJECT BACKGROUND

Shell Eco-marathon is an international competition organised by Royal Dutch Shell aiming to develop cleaner energy solutions and social responsibility among younger generations, providing students with the opportunity to design, manufacture and race ultra-energy-efficient vehicles, with safety and environmental sustainability being of primary focus. The Shell Eco-Marathon Europe event had been scheduled to take place at Mercedes Benz World in Weybridge, Surrey from June 27 to July 3, 2020, before it was cancelled due to unforeseen circumstances (Shell Eco-marathon, 2020).

Competition Structure

The Shell Eco-marathon event is comprised of the Prototype Class and the Urban Concept Class. Urban Concept vehicles resemble modern passenger cars in appearance. The main objective for this class is to develop technologies that could be more readily implemented in road vehicles to improve their energy efficiency. In contrast, the Prototype Class provides a greater degree of flexibility, focusing less on the immediate application of technology but more on encouraging innovative solutions that result in some of the most energy efficient vehicles of any class in the world, as shown in Figure 2.



Figure 2 - Duke Electric Vehicles Prototype entry. 14,573 mpg equivalent (Guinness World Records, 2018)

Project Aims and Objectives

Imperial Racing Green’s previous entry to the Shell Eco-marathon Prototype Class had not met all the regulations specified by the competition organisers. **The principal aim for this project was therefore to develop a vehicle, in conjunction with DMT Group 27, that would pass all the regulation criteria and compete under the Prototype Class at the Shell Eco-marathon Europe event.** This team designed, manufactured and tested the vehicle’s chassis and steering system while DMT Group 27 developed its powertrain. To ensure that this new vehicle would pass the extensive scrutineering process, the Shell Eco-marathon official rules (Simmons, 2020) were carefully considered. As well as this, three general project objectives (Table 1) were defined to guide the Product Design Specification (Table 2).

Table 1 - project objectives

OBJECTIVES
1. <i>Design a chassis that will comfortably fit an average female driver, provide mounting points for all components and be mounted to the existing aerodynamic shell with minimal modifications.</i>
2. <i>Design a steering system which maximises efficiency and provides an adequate level of feedback to the driver, allowing for adjustments to be made to the front wheel alignment.</i>
3. <i>Implement a powertrain interface on the developed chassis that will be compatible with the developments of Powertrain DMT Group 27.</i>

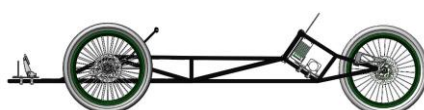


Table 2 - Product Design Specification

Aspect	Statement / Criteria	Verification Method
Design Constraints		
Dimensions		
Vehicle track width	At least 500 mm, between outermost contact points of tyres and the ground (Article 39 b))	Measurement
Ratio of height to track width	Less than 1.25 (Article 39 c))	Measurement
Vehicle wheelbase	At least 1000 mm (Article 39 d))	Measurement
Vehicle width	Less than 1300 mm (Article 39 e))	Measurement
Vehicle length	Less than 3500 mm (Article 39 f))	Measurement
Frame size	Should fit a female driver with body dimensions greater than 50% of the average population	Demonstrated in CAD
Vehicle body		
Chassis weight	At least 10% lighter than previous chassis	Measurement
Vehicle deflection	Maximum allowed deflection should not affect vehicle operation	Testing
Vehicle serviceability	Internal components should be readily accessible and shell easily removable	Inspection
Rear compartment	Easily accessible for inspection of powertrain and to reset joulemeter	Inspection
Bulkhead	Upright rigid partition must separate propulsion system from driver compartment Wheels located inside the body must also be separated by a bulkhead.	Design review
Driver compartment	Driver must be able to escape in less than 10 seconds (Article 30 a))	Testing
Steering and Brakes		
Wheels	Must not come into contact with the body of the vehicle at any steering angle	Inspection and testing
Turning radius	Must be front wheel steered and have a minimum turning radius of 8 m or less (Article 42 a), b))	Testing
Steering set-up	Wheel angle (toe and camber) must be adjustable to +/- 3° from favoured set up, with an accuracy of 0.5°.	Testing
Brakes	Must provide appropriate mounting for brake callipers	Design review
Pedal box	Must provide appropriate mounting for pedal box	Design review
Safety		
Chassis solidity	In the event of rollover or collision the chassis will safely protect the driver's body (Article 26 a))	Design review
Crumple zone	Minimum crumple zone of 100 mm between the front of the vehicle and the driver's feet (Article 25 a) ii.)	Design review
Visibility	Driver must have a direct arc of visibility ahead, to 90° on each side (Article 28 a)) and +/- 15° vertically.	Testing
Mirrors	Provide mounting points for two rear-view mirrors, one on each side of the vehicle	Design review
Safety belts	Provide at least five mounting points for safety harness on the vehicle's main structure that can each withstand 200 N (Article 29 a), d))	Testing



Emergency extraction	Cabin must be easily accessible and opened from the inside and outside (Article 30 c))	Inspection
Propulsion system isolation	Bulkhead must provide effective isolation of battery/motor compartment (Article 27 a))	Testing
Stress safety factor	Minimum safety factor of 1.2	Design review
Manufacturing Constraints		
Time constraint	Manufacturing must be completed by week commencing 2 nd March	Gantt chart progress analysis
Budget constraint	Upper bound for project budget is £5000	Design review
Suppliers and manufacturers	Use internal or approved external suppliers where possible	Design review
Materials	Ensure that components can be mostly manufactured in house Ensure correct risk assessments and precautions are taken for toxic materials	Design review
Performance		
Service life	Vehicle must withstand at least 5000 km of driving distance before major maintenance	Design review

Shell Eco-marathon Team

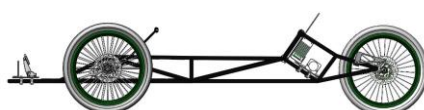
Individual roles and responsibilities were assigned to each team member according to their previous experiences as well as areas of interest. These are summarised in Table 3. The successful progression of this project was also supported by members of staff and other members of the Shell Eco-marathon team at Imperial Racing Green, summarised in Table 4.

Table 3 - team members and roles

Team Member	Roles	Responsibilities
Carlos Firgau	Team Lead Analysis Lead Conceptualising Lead	Vehicle Dynamics Analysis, Conceptual Design
Asad Raja	Report Manager Team Secretary Prototyping and Testing Lead	Report Writing, Time Management, Stress Analysis
Jessica Eichel	Engineering Drawing Lead Budgeting Lead Embodiment Lead	Engineering drawings, Sketching, Budgeting
Rahman Al-Shabazz	CAD Lead Manufacturing Manager	CAD modelling, Manufacturing, Stress Analysis

Table 4 - external Shell Eco-marathon team

Name	Roles	Contact
Dr Alexis Ihracska	Project Supervisor	a.ihracska@imperial.ac.uk
Dr Marc Masen	Project Co-Supervisor	m.masen@imperial.ac.uk
Sampson Tam	SEM Team Principal	sampson.tam17@imperial.ac.uk
Muntadhar Mahmoud	SEM Chief Mechanical Engineer DMT Group 27 Team Lead	muntadhar.mahmoud17@imperial.ac.uk
Tom Mrazek	SEM Chief Aerodynamics Engineer	tomas.mrazek17@imperial.ac.uk



CHASSIS DESIGN

The term chassis describes the frame of a vehicle. It is responsible for providing secure locations for and support to all vehicle components; strength and stiffness to resist all vehicle loads; and for providing a structure that both accommodates and protects the driver (Al-Shabazz et al., 2020b). The key design improvements in reflection of the previous entry's chassis were to increase maximum allowable driver height to 5' 5" and to increase the ride height to 150 mm for better aerodynamic performance as set by project leads. Additionally, the chassis would have to meet the requirements outlined in Table 2, including the goal to achieve a 10% reduction in weight on comparison to the previous entry.

Design Development

Wheelbase and Track Width

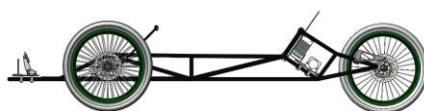
According to the official rules of the Shell Eco-Marathon competition (Simmons, 2019) the track width of the Prototype Class car is defined as "the distance between the midpoints where the tyres of the outermost wheels touch the ground". While there is no explicit definition for the wheelbase, the standard definition refers to the distance between the front and rear axles of the car.

The previous version of the Shell Eco-Marathon car was designed for a 4' 8" tall driver (1.42 m tall) and was measured to have a wheelbase of 1450 mm and a track width of 500 mm. These measurements had to be revised to meet the driver height objectives of this project.

Wheelbase Selection

Previous results (Santing et al., 2007) indicate that the effect of wheelbase on the tyre drag value when cornering is negligible, although a longer wheelbase means that an increased number of components and materials are required to build the car which results in increased mass and friction drag. However, using a shorter wheelbase can also produce negative results as it may induce flow separation on the vehicle's shell. After consulting with the project supervisor, it was decided that the best method for selecting an appropriate wheelbase was to choose a value that was as small as possible, to decrease total mass, while still being able to comfortably and safely house all the components of the car as well as the driver. Comprehensive computational validation and testing of prototypes in a wind tunnel were not conducted as these were outside the scope of this project.

Lengths were recorded for different sections of the vehicle from the previous chassis from which the total approximate wheelbase was determined. To minimise the amount of material used in the steering system, particularly in the steering column mechanism, the driver was positioned so that their hands are as close as possible to the front wheels, without the legs extending too far forward. Different configurations were discussed until the final arrangement was selected shown in Figure 3.



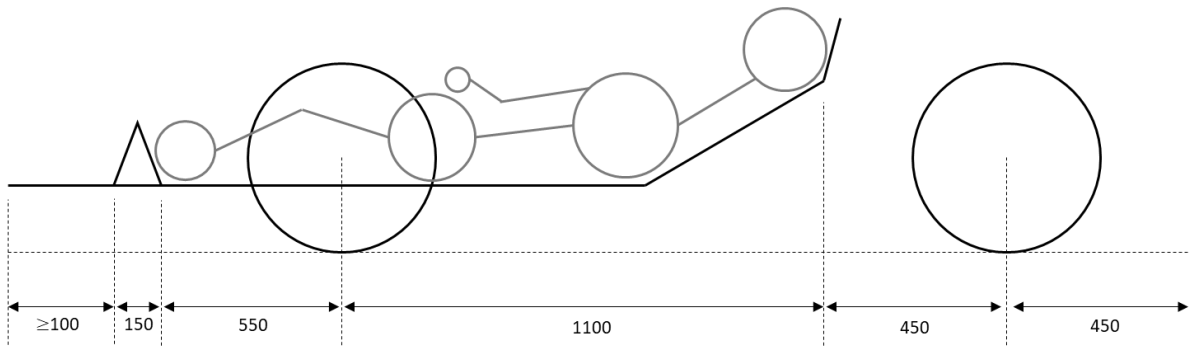


Figure 3 - length dimensions between key points

Accommodating a 5' 5" driver required the wheelbase of the vehicle to be increased slightly to 1550 mm. Even though the increase in driver height was significant, a comparatively smaller increase in wheelbase was achieved due to slight changes to the sitting position of the driver.

Track Width Selection

The selection of the track width for this vehicle was important as an inappropriate value could result in rollover of the vehicle which is one of the most common types of accidents observed in fuel economy racing. This is especially true for 3-wheeled designs due to their inherently lower stability (a 4-wheel design was discarded early on in this project as it would not fit into the teardrop shape of the existing shell and also because it would increase the number of parts required which would lead to an unnecessarily heavy car). Studies carried out by the ETH Zurich PAC-II team (Santing et al., 2007) also found that aerodynamic drag increases with track width and accounts for approximately 50 % of the total drag generated. Therefore, keeping the track width to a safe minimum became an objective.

Rollover Calculations

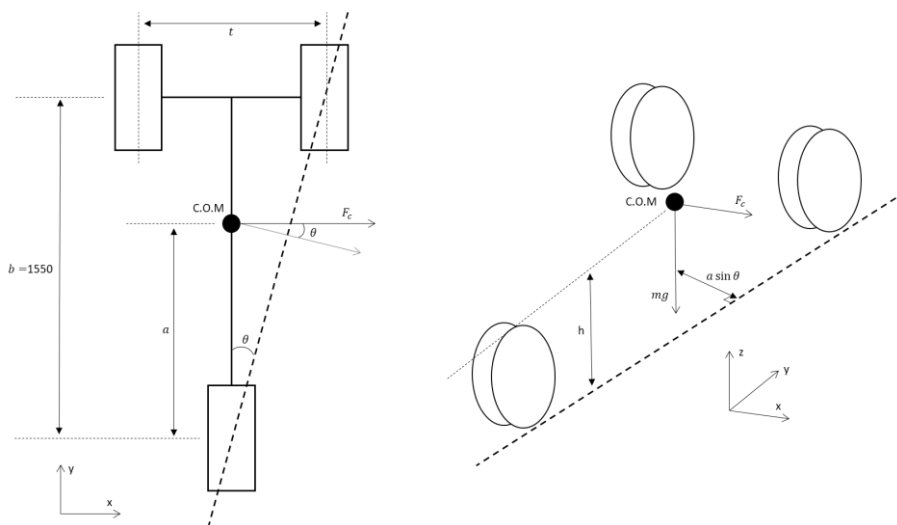
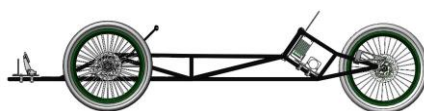


Figure 4a - axis of roll, 4b - frictional roll load component

Calculations were carried out to determine the approximate minimum track width to prevent rollover that would be required for a vehicle operating in the Shell Eco-Marathon race conditions. Collisions



for a low speed fuel efficiency race were considered unlikely and, therefore, the main mechanism for rollover investigated was that occurring due to the vehicle attempting to turn at a very high velocity. In this case, the axis about which the vehicle would roll is the line joining the rear wheel to one of the front wheels, as shown in Figure 4a. The instant at which the car begins to roll is when the normal reaction of the inside wheel, R_{NF} , is zero.

In a rotating frame of reference, the centrifugal force is equal in magnitude to the friction acting between the tyres and the road, characterised by the coefficient of friction μ . Only a component of this which is perpendicular to the rollover axis would cause rollover, as shown in Figure 4b.

The angle θ which is the direction in which this force component acts, can also be related to the track width, t , of the car as well as its wheelbase, b , as follows.

$$\tan \theta = \frac{\frac{1}{2}t}{b} \quad (1)$$

A balance of moments about the rollover axis at the instant the car begins to roll over, as shown in Equation 2, allows the angle θ to also be related to the distance of the centre of mass of the car from the rear axle when viewed from above, a and the vertical height of the centre of mass above the surface of the track, h . The acceleration due to gravity is represented by g .

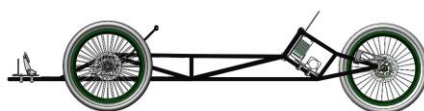
$$\mu mg \cos \theta h = mga \sin \theta \quad (2)$$

$$\therefore \tan \theta = \frac{\mu h}{a} \quad (3)$$

Equating both expressions of $\tan \theta$, it was possible to obtain an expression for the minimum track width necessary for the car to avoid rolling over.

$$t = \frac{2bh\mu}{a} \quad (4)$$

From this steady state turning analysis, an estimated minimum track width was calculated using a wheelbase, b , of 1.55 m. The height of the centre of mass, h , was estimated to be approximately $\frac{2}{3}$ of the radius of the wheel (250 mm) – an acceptable assumption as the majority of the driver's body was expected to sit below the plane of the centres of the wheels in the final design. μ was approximated to be 0.75, a realistic estimate for the tyres available in the Pit Garage which have a lower quality of rubber compound compared to the Michelin 45-75R16 used by ETH Zurich which had a μ of 0.8 (Santing et al., 2007). a was taken to be approximately $\frac{1}{3}$ of the wheelbase, measured from the front axles – an acceptable assumption since the majority of the driver's body was expected to be closer to the front wheels ($\frac{1}{3}$ is proven to be an acceptable approximation in the 'Spaceframe Deflections and Stresses' section, where an a value of 0.42 was calculated). A minimum acceptable track width of 381 mm was obtained.



In this analysis, the minimum trackwidth is independent of the velocity and turn radius of the car. The underlying assumption is that the turn is taken at the maximum velocity allowed by the grip of the tyres – any higher cornering velocity would only cause the vehicle to slide instead of rolling over.

It is evident that the minimum track width necessary is significantly below the 500 mm minimum allowed by the rules. To avoid an unwanted drag penalty, a value of 500 mm was selected. In practice, this meant that a maximum ratio $\frac{h}{a}$ of 0.215 could be imposed on the design of the chassis to ensure that this trackwidth would prevent rollover for the wheelbase and μ stated previously.

Different Types (monocoque, spaceframe, ladder, backbone)

Following from the research on loading cases during operation of the vehicle, the next step was to decide whether a ladder, monocoque or spaceframe chassis design would be best suited for a successful design.

Ladder

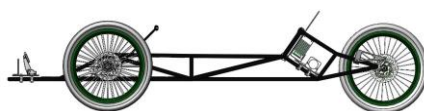
The most basic chassis structure is the ladder frame design, named after its resemblance to a conventional ladder (Waterman, 2011). This structure is built from two members that run parallel through the length of the vehicle, connected by multiple members perpendicular to the chassis direction. This design dates back to horse-drawn carriages, traditionally made from wood. However, its poor torsional stiffness made it unsuitable for this car.

Monocoque

A monocoque chassis design carries the potential for a stiffer and stronger chassis structure (Seward, 2014). It makes use of plates and shells loaded in shear to construct a closed box that acts as a protective outer body work with a rigid internal structure that is able to carry all loads. The benefit of using entire panels and shells is a higher polar moment of inertia in the longitudinal direction. This reduces torsional stresses (Waterman, 2011) which promotes better handling and a safer design.

With a high material consumption, special material composites are often used to reduce the compromise on weight. Carbon fibre composites have recently been introduced as a means of enabling a lightweight, smooth yet strong structure. The manufacturing process for carbon fibre composites is complex. The first step is to create a full-size mould of the chassis using wood or a resin. With this mould made, there are two approaches to completing the monocoque shell (Seward, 2014).

1. Wet lay-up – applying alternating layers of carbon fibre and resin to the mould and allowing to cure in a vacuum bag before detaching from the mould.



2. Pre-Impregnated (Pre-preg) – applying a premade carbon fibre-resin reinforcement to the mould and allowing to cure in a vacuum bag inside an autoclave before detaching from the mould. Generally, this process generates the lightest and strongest monocoque designs.

Spaceframe

The spaceframe design involves creating a 3D structure from tubes. By ensuring all members are joined at nodes with the use of diagonal members to form triangles, stresses can be reduced by at least one order of magnitude (Waterman, 2011). Any loads on the structure should then be applied primarily at nodes. This is to ensure that all members in the structure are loaded in pure tension or compression. Depending on the material, joining techniques that may be applied between members include welding, carbon fibre wet lay-ups and internal or external lugs. The driver's seat in a spaceframe structure is comprised of floor panels attached between the spaceframe members.

Selection

With a low torsional stiffness, the ladder approach was deemed unviable for the chassis. The monocoque design was ruled out immediately as no vacuum bag or autoclave sufficiently large to enclose a full chassis structure were available on-site. Both, the wet lay-up and the pre-preg process would have had to be outsourced – a costly approach. Therefore, it was concluded that a spaceframe design was the most suitable option. A dual support member structure was preferable over a backbone structure as the loads experienced on the chassis would be distributed across two members rather than one (Al-Shabazz et al, 2020b). As well as this, due to the material selection of carbon fibre made further into the development of the chassis to minimise the overall weight, the backbone structure was not appropriate as it would require all members to be joined to the single backbone structure – a configuration that favours welding. Carbon fibre cannot be welded and so would have raised difficulties while manufacturing.

Materials Selection

The Shell Eco-Marathon is a fuel efficiency race where a high strength to weight ratio is desirable in order to travel furthest on the fuel supplied whilst withstanding the load condition. Other desirable as well as regulated criteria are the chassis' ability to withstand a 700N force at its roll bar (bulkhead), designed to protect the driver in the event of rollover, and for the chassis to experience minimum deflection.

Materials Selection of Spaceframe Chassis

The properties and potential of metals and carbon fibre for building a spaceframe are given in Table 5.

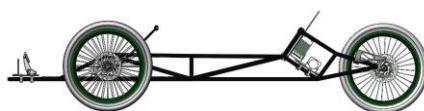


Table 5 – Potential of various materials for the spaceframe

Material	Youngs modulus (GPa)	Yield strength (MPa)	Density (g/cm3)	Comments
SAE ASU 4340 Steel	200	470	7.85	Easily machined using all conventional techniques Not available as tube Too heavy
IOM Steel Tube	200	496	8	£2.50 per foot Too heavy
4130 Chrome moly	205	517	7.85	£8.50 per foot Requires pre and post welding treatment Too heavy and complex to manufacture
Docol Tube R8	200	690	7-8	Easily welded Higher specification than required Expensive and heavy
Carbon Tubes	90	Varies with tube	1.6	Connect using joining techniques in Table 7 £20 per metre Circular or square tubes
Aluminium	72	35	2.7	£13.47 per m Can be easily welded and machined Various shaped tubes

Carbon fibre and aluminium were evidently the most suitable choices given their low density, ease of joining by welding or numerous carbon fibre joining techniques, and availability to purchase. To help inform the design decision, tube shapes of both materials were analysed next.

Square vs Round Profile

One decision to consider was the use of square vs round tubes. A simple calculation was used to compare the mass per unit length of the two cross sections shown in Figure 5 (note the discrepancy in thickness analysed reflecting the purchasing options available). At the time of analysis, carbon fibre and aluminium were the two most favourable materials and so were further analysed.

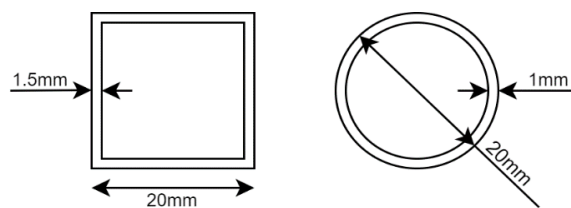
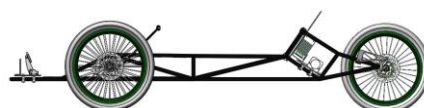


Figure 5 - analysed cross-sections

The results (Table 6), showed that a circular cross-section would be highly beneficial from the weight reduction perspective. The carbon fibre tubes also displayed a 40% weight reduction compared to the aluminium equivalents, increasing efficiency.

Table 6 – Comparison of square and circular tubes

	Square		Circular	
	Carbon Fibre	Aluminium	Carbon Fibre	Aluminium
Mass (kg/m)	1.776	2.997	0.955	1.612



Aluminium would require cutting and spot welding to create a spaceframe, while carbon fibre would require one of the techniques in Table 8. Due to health concerns within Imperial College London, welding would be problematic. Therefore, it was decided to use round carbon fibre tubes for the spaceframe. This was also more cost effective, with round tubes costing £8 less per metre than their square tube equivalent (Easy Composites, 2019).

Connection Method for Spaceframe

The two fundamental joining options for the carbon fibre spaceframe tubes were as shown in Table 7.

Table 7 - Joining methods for carbon fibre tubes

Joining Method	Process	Comments
Carbon fibre wet layup around held together tubes	Hold together with a jig and wrap joints with carbon fibre pre-preg or carbon fibre fabric with an applied epoxy resin mixture.	Jig is cost and labour intensive. Difficult to ensure angles correct for more complex spaceframe geometry.
Lugged tube connectors	Join using lugs made from carbon, steel or titanium.	Angular arrangement of tubes limited by connector available.

A weight analysis was carried out on a basic chassis design (Figure 6) to explore the effect of both connection types. The analysis was based on steel connector lugs that were available as the cost to externally source customised carbon, aluminium or titanium lugs would exceed the budget.

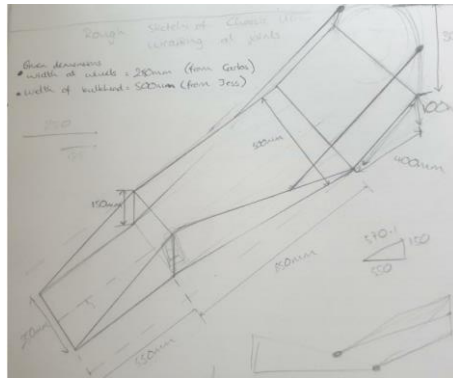
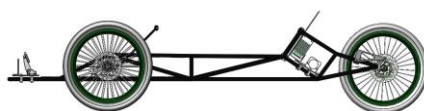


Figure 6 - weight analysis spaceframe model

The analysis revealed that using steel connectors would result in a chassis weight of approximately 14.4 kg, with over 85% of that weight coming from the weight of the steel connectors. Alternatively, the weight of the chassis using the carbon fibre wet lay-up connection method was found to be approximately 3.0 kg. Thus, the wet layup method was pursued for further design developments.

Analysis and testing of prototype joints supported the use of carbon fibre tubes with wet lay-up joining. The joining method was developed to use 3-D printed polymer lug inserts for alignment of members around joints instead of a jig. This allowed for a more complex spaceframe design.



Panel Materials Selection

The floor and back panels provide support for the weight of the driver, separate the driver from the rear compartment and shell floor, and are used to mount the pedal box. Table 8 shows suitable panel materials which are readily available, simple to manufacture into the required shape, have low density and have acceptable specific strength and stiffness.

Table 8 - Sheet materials and properties considered for panels

Material	Mechanical Properties	Ease of Fabrication	Cost	Weight
Aluminium Sheet	Low density for metal	Very easily machinable using all conventional tools	~£40/sqm	11kg / sqm
Carbon Aluminium Sandwich Panels	Lightweight, stiff Low longitudinal modulus High transverse shear modulus	Can be manually cut. Ensure safety precautions are followed for carbon fibre	~£300/sqm	2.95kg/sqm
Carbon Foam Core Sandwich Panels	Lightweight, stiff High longitudinal modulus Low transverse shear modulus	Can be manually cut. Ensure safety precautions are followed for carbon fibre	~£180/sqm	2.71kg/sqm

Carbon sandwich panels with a closed-cell PVC foam core were selected for the floor panels, due to their high stiffness and lower cost and density than aluminium cored panels or aluminium sheets, (Figure 7).

The roll bar or bulkhead was made of a 4 mm aluminium plate, to ensure it would endure a rollover impact and a 700 N force from all directions. It is also fire retardant, which was a race requirement to ensure safety since it would separate the powertrain compartment from the driver.

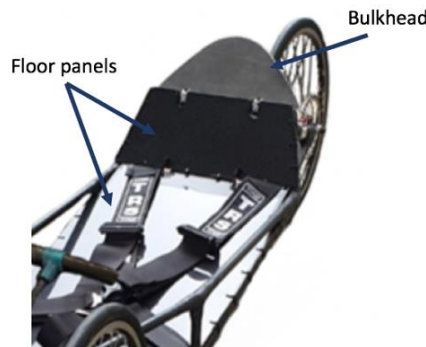
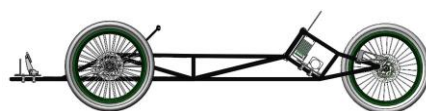


Figure 7 - floor panel and bulkhead locations

Spaceframe Joint Material Corroboration

Carbon fibre fabric with an applied epoxy-resin mixture was used for the wet-layup spaceframe joining method as opposed to carbon fibre pre-peg which would require the use of an autoclave. Carbon fibre reinforced polymers are composite materials where the carbon fibre provides the strength and stiffness while the polymer, usually an epoxy resin matrix, transmits loads to the fibres and protects and holds them together (Fekete, 2017). Long strands of carbon filament are grouped together and bonded with an epoxy resin matrix to form a laminate. A laminate is strongest when loaded in the fibre orientation, hence multidirectional weaving patterns can increase the torsional



stiffness, flexural rigidity and tensile strength. Multiple laminates are layered together in a compact structure which minimises voids, providing a very light, strong and fatigue resistant component.

Table 9 shows the Young’s modulus and thermal expansion coefficient for different composite materials with potential in high strength and low weight applications (King, 1989).

Table 9 - Youngs modulus and thermal expansion coefficient for composite materials

Material	Young’s Modulus (GNm ⁻²)	Thermal expansion coefficient ($\alpha \times 10^{-6} \text{ } ^\circ\text{C}^{-1}$)
Carbon fibres – along fibre	200-800	-0.1–1.2
Carbon fibres – perpendicular to fibres	10-20	7-12
Glass fibres	76	4.9
Epoxy resins	3-6	70
Polyester resins	2-4.5	100-200
Carbon fibre / epoxy unidirectional laminae – parallel to fibres	220	-0.2
Glass fibre / polyester unidirectional laminae – parallel to fibres	38	11

It is evident that carbon fibres bonded with an epoxy resin matrix have a much higher Young’s modulus than glass fibre with a polyester matrix. Carbon fibres also have a much lower thermal expansion coefficient, corroborating them as suitable for automotive use where heat from tyre friction and the powertrain raises temperatures.

Factors affecting strength

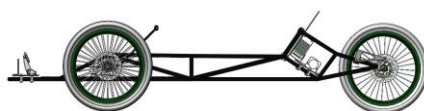
The strength of a carbon fibre reinforced polymer component is particularly sensitive to interface bonding. Greater interface bonding arises from stronger adhesion of the epoxy matrix with the fibre, achieved by ensuring carbon strands are fully covered with epoxy resin to prevent voids forming.

Failure modes

Although carbon fibre epoxy composites typically have a very long fatigue life and can withstand many cycles of stress before failure, the structures can vary and will dictate if and how a component will fail. During loading and repeated use, stress will accumulate, the fibre matrix interface will weaken the bonds, and any voids present will act as microcracks and grow. This can lead to failure mechanisms such as fibres bending, buckling and fracturing or failure of epoxy matrix. The amount of damage accumulated depends on the matrix properties and the strength of the reinforcing fibres.

Risk Assessment

Having a carbon fibre-based design meant that the team would be working with processes seldom used by other DMT groups. Thorough research was conducted to ensure that the project was completed with the necessary safety equipment and precautions. These precautions were outlined in relevant risk assessment forms that explored the dangers of working with carbon fibre and resins. Each team member completed a mask fitting test and briefing with a safety officer at Imperial.



Prototype Testing

Wet Layup Test of Joints

The objective of performing multiple prototype tests was initially to test the feasibility of the wet layup method to connect carbon fibre tubes together. It was found that by careful preparation of surfaces to increase adhesion, and optimising the amount of fibre and epoxy used, the joints would cure with the strongest matrix bonds. Prototyping helped the group finalise the process used.

The prototypes produced are shown in Table 10. Straight membered joints were made by clamping the tubes in place. Angled dual member joints were also made to test the feasibility of more complex geometries. However, clamping the tubes accurately for complex geometries was found to be problematic. Therefore, plastic lug inserts were prototyped using the UPS Mini 3D printers in the Imperial College Advanced hackspace and inserted before joining to align two tubes in a 90° joint.

Table 10 - Joints prototyped

Prototype Class 1: Straight Joint	Prototype Class 2: Angled Joint without Lug	Prototype Class 3: Angled Joint using 3D Printed Lug Insert
 <p style="text-align: center;">Figure 8a</p>	 <p style="text-align: center;">Figure 8b</p>	 <p style="text-align: center;">Figure 8c</p>

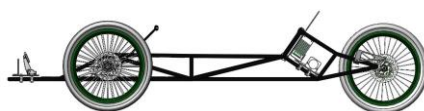
Improvements and Optimisation

Cutting and filing of tube profiles such that tubes sat flush at joints and covered the lugs completely was considered. However, prototypes showed that the effect of a slightly exposed lug was minimal, and that the strength of the joint was more dependent on the wrapping and layup around it.

Cutting strips from a large sheet of carbon fibre weave was found to be too delicate to manually handle. Therefore, rolls of woven carbon fibre pre-cut to widths of 25 and 50mm with secured edges were purchased, helping to prevent misalignment and fraying during layup. Since a vacuum bag could not be used for such a large assembly to tightly cure the layup, a composite shrink tape was used instead, which was wrapped around joints and shrunk on heating. It was important to apply the correct amount of resin – too much and there was unwanted liquid during wrapping causing excess slip between layers; too little and bonds did not fully cure.

3 Point Bending Test: test joint vs plain tube

After prototyping a straight carbon fibre tube joint as shown in Figure 8a, a 3-point bending test was conducted using the Instron-3366 testing machine (Figure 9). A 3-point bending test was also carried out on plain carbon fibre tubes under the same test conditions for comparison. The results are shown



in Figure 10 as force-deflection graphs. The aim of this test was to calculate and compare the Young’s Modulus and yield strength of a joint section and that of a plain tube. These material properties were needed for stress and deflection calculations on the spaceframe.

Method

1. The 3-point bending test blocks were attached to the Instron test machine, as shown in Figure 4.
2. The test specimen was placed on the supports, making sure it was straight and that the centre of the joint sat directly underneath the load head.
3. The machine loading was started, and recordings were taken of the load and deflection values at a rate of 10 samples per second.
4. The test was repeated for two plain carbon tubes without a joint.
5. Load versus deflection graphs were plotted for each test and used to calculate Young’s Modulus and yield strengths for both the joint section and a plain tube.

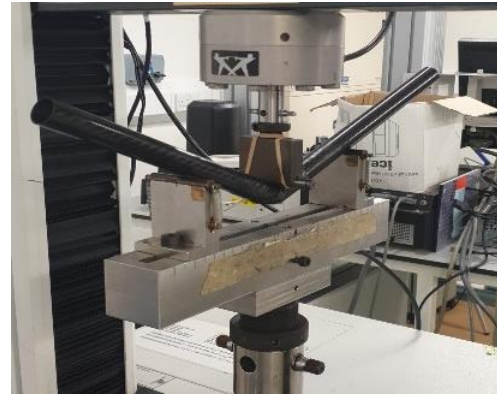


Figure 9 - 3-point bending on test joint

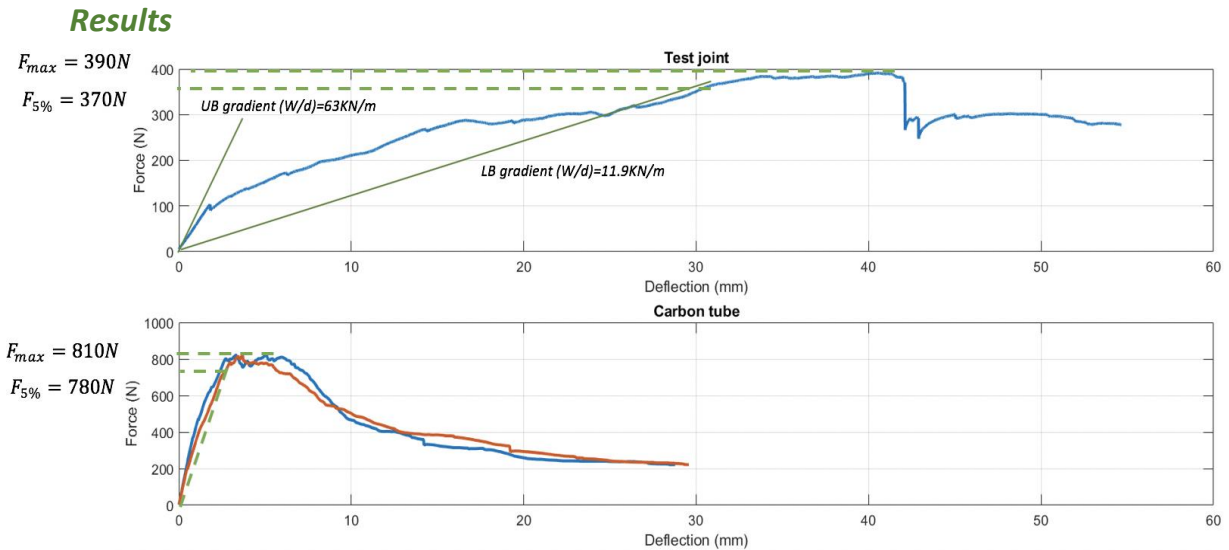
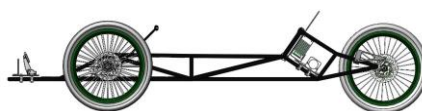


Figure 10 – graphical analysis from bending tests

Interpretation of Results

According to the ISO 13586:2000 standard, linear elastic fracture mechanics can be used for a 3-point bend test of a composite specimen if the non-linearity of the load-displacement line is less than 10%, as described by Equation 5.

$$\frac{F_{max}}{F_{5\%}} < 1.1 \tag{5}$$



The force-deflection graphs show that the plain carbon tubes satisfy this criterion, and therefore linear elastic fracture mechanics was used to analyse approximately the yield strength and Young’s Modulus (Table 11). For the wrapped test joint, the graph did not show fully linear loading. Instead, to approximate the loading as linear, upper and lower bound loading lines were drawn. For Equation 5 to hold true, and to give the most conservative values of yield strength and Young’s modulus, the lower bound value of 11.9 KNm⁻¹ was used as the gradient of the test joint.

Table 11 - 3 point bending test results

	Calculation	Plain Carbon Tube (average of two)	Test Joint
$P_{max} (N)$	Maximum value on graph	810	390
Maximum Bending Moment (Nm)	$M_{max} = \frac{P_{max}L}{4}$ $P_{max} = UTS$ $L = 0.15 m$	40.5	19.5
Yield Stress (MPa)	$\sigma_y = \frac{My}{I}$ $I = \frac{\pi}{4}(0.01^4 - 0.009^4)$	153.6	71.8
Gradient (KN/m)	$Gradient = \frac{\Delta F}{\Delta d} = \frac{W}{\delta}$	385	11.9
Youngs Modulus (GPa)	$\delta = \frac{WL^3}{48EI}$ $E = \frac{gradient * L^3}{48I}$	23.86	0.734

Conclusions

The yield strength of the tube with the test joint was found to be half that of a plain carbon tube and the Young’s Modulus of the test joint was also considerably lower. As the test joint was the first prototype produced, likely causes are the failure modes and factors affecting strength mentioned previously such as poor adhesion and insufficient epoxy matrix applied. Future joints followed a sophisticated layup method as described in the ‘Manufacturing of Spaceframe’ section.

Final Design Process

Powertrain Interface

An early design decision that had to be made in order to avoid inconsistency and conflict with design decisions made by the Powertrain DMT team was the nature of the chassis’ interface with powertrain components. The powertrain interface would be concerned with the design of the chassis’ rear section behind the bulkhead, positioned just behind the driver’s head. To make a start on the conceptualisation, measurements (Figure 11) of the previous entry were taken (Table 12) to define the approximate dimensional scale of the rear chassis section.

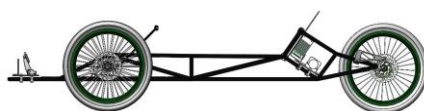




Figure 11 - powertrain interface measurements

Table 12 - powertrain interface measurements

Measurement	Value (mm)
Bulkhead Width	400
Bulkhead Height	300
Bulkhead to Axle	500

It was clear that the width of this section would have to narrow from the bulkhead to the axle to ensure that it could fit within the teardrop shape of the shell. The width of this rearmost part would therefore be constrained by the rear axle length. This dimension, as well as all the other relevant information that was obtained from the Powertrain DMT team, is summarised in Table 13. Many of these final dimensions were derived through design iterations by the Powertrain team based on mutually informed decisions. Early meetings with the Shell Eco-marathon Team Principal revealed that one of the improvements that this chassis design should make upon the previous was a less cramped rear section to allow for easier access to and assembly of the powertrain components.

Table 13 - powertrain interface dimensions

Powertrain Parameter	Value
Components	Battery, Motor, Motor Controller, Axle
Type of Drive	Chain
Axle Dimensions	10 mm diameter, 135 mm long
Motor Dimensions	52 mm diameter, 235 mm long
Battery Dimensions	390 mm x 70 mm x 110 mm
Motor Controller Dimensions	80 mm x 80 mm x 30 mm
Motor Speed	600 rad/s

General Powertrain Interface Design

Five different configurations were conceptualised for the powertrain interface design. These are summarised in Table 14 along with their relative merits and drawbacks.

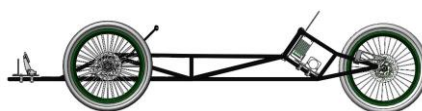
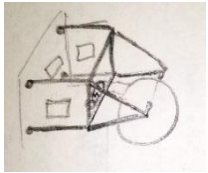
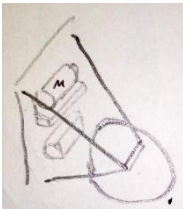
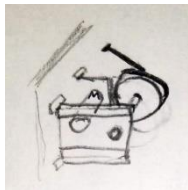
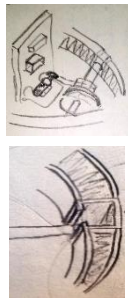
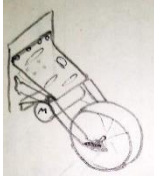
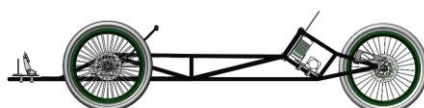


Table 14 - conceptualised powertrain interface designs

Configuration	① Two-Section Rear Spaceframe	② Simple Rear Spaceframe	③ Panel Design	④ Axle Mounted to Shell	⑤ Aluminium Sheet Mounting Plate
Explanation	The rear spaceframe extends from the bulkhead in a large cube structure. Mounting plates can be attached between members in this section. Members extend from this section in a narrowing triangular shape to the axle.	The rear spaceframe extends from the bulkhead into a narrowing triangular structure to the axle. Components are mounted to the back of the bulkhead.	Brackets extend from the back of the bulkhead and plastic panels are attached to them. The motor and axle are mounted between the plastic panels and other components are mounted to the panels.	The axle is mounted directly to the shell at a hollow slotted section in the shell's sandwich panel. Components are mounted to the back of the bulkhead, with a short protruding mount for the motor.	An aluminium sheet is bent around a transverse member in the rear spaceframe. Components are mounted to the aluminium sheet and the motor is mounted to the transverse member.
Sketches					
Pros	<ul style="list-style-type: none"> - Lots of space for mounting of components. - Similar to the previous entry so mounting panels can be reused. 	<ul style="list-style-type: none"> - Saves weight and space. - Reduces number of joints – easier to make and less chance of misalignment. 	<ul style="list-style-type: none"> - Minimises number of joints – easier to make and less chance of misalignment. - Plastic panels easy to manufacture and metal brackets readily available. 	<ul style="list-style-type: none"> - Saves weight and space. - No joints – easier to make. 	<ul style="list-style-type: none"> - Lots of space for mounting components. - Can design sheet to mount everything compactly whilst using cut outs to save weight.
Cons	<ul style="list-style-type: none"> - Required many joints which may introduce misalignment. - May be too large to fit into shell. - Unnecessary weight and space contribution 	<ul style="list-style-type: none"> - May not be enough space to mount all the components. 	<ul style="list-style-type: none"> - Unnecessarily complicated motor mounting that does not make use of its foot mount bracket. - May be too large to fit into the shell. 	<ul style="list-style-type: none"> - May prove difficult to mount the axle in the shell due to its curved shape. - Cutting the sandwich panel may be challenging. - May not be enough space to 	<ul style="list-style-type: none"> - Bending of the aluminium sheet may be an inaccurate process.



				mount all the components. - Flexing of shell due to loads may lead to chain misalignment.	
--	--	--	--	--	--

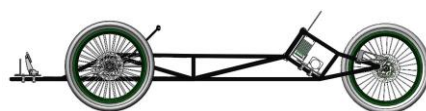
Using the Product Design Specification as a guideline, each idea was evaluated using a decision matrix with the following four categories: space for mounting all components whilst fitting in shell, weight, reliability of chain alignment and ease of manufacture.

Weightings were assigned to each category from 1 to 4, with 4 signifying the most important category for the application. Each idea was then ranked from 1 to 5, with 5 being assigned to the idea that best fulfils the requirements of each category. The decision matrix is shown in Table 15.

Table 15 - morphological analysis of powertrain interface designs

Criteria	Weighting	Option 1		Option 2		Option 3		Option 4		Option 5	
		Score	Weighted Score								
Space	4	2	8	4	16	1	4	3	12	5	20
Weight	1	1	1	4	4	2	2	5	5	3	3
Reliability of Chain Alignment	3	3	9	4	12	2	6	1	3	5	15
Ease of Manufacture	2	3	6	5	10	2	4	1	2	4	8
		Total 1:	24	Total 2:	42	Total 3:	16	Total 4:	22	Total 5:	46

This shows that design options ② and ⑤ were the best out of those considered. These designs were therefore integrated and developed. Specifically, a transverse member was added to the simple rear spaceframe of concept ② and the aluminium sheet of concept ⑤ was replaced with a mounting plate for the motor, with the battery mounted to the back of the bulkhead. The developed concept was integrated with the rest of the spaceframe as shown in Figure 12. This sketch shows a slotted rear axle mount component, which was considered in order to offer adjustment of the axle position such that the chain could be tightened. In the final powertrain interface design shown in Figure 13, this has been removed as chain tightening was instead offered by slots in the motor’s foot mount bracket designed by the Powertrain DMT team. The final design also developed the rear spaceframe structure further such that the rear-most spaceframe point where the axle was to be mounted was made to be a node of the spaceframe, to allow for better stress distribution.



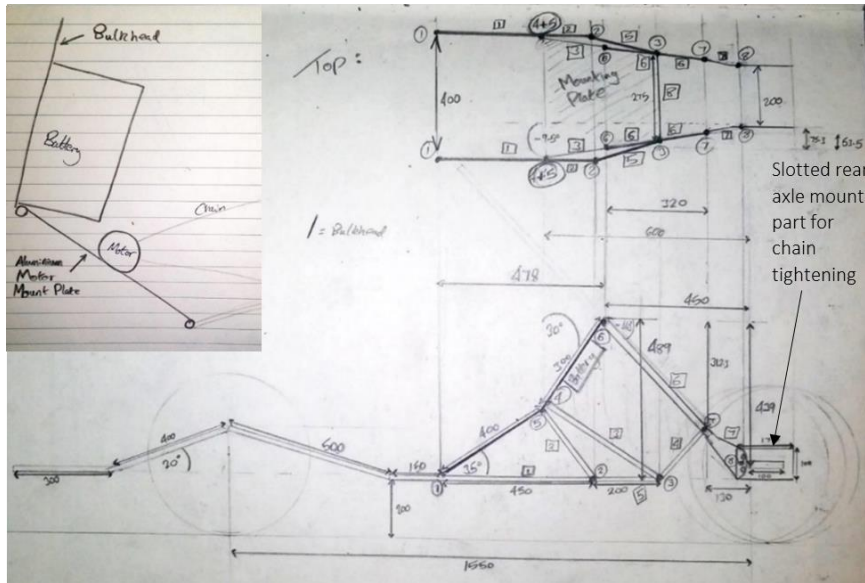


Figure 12 - powertrain interface developed design

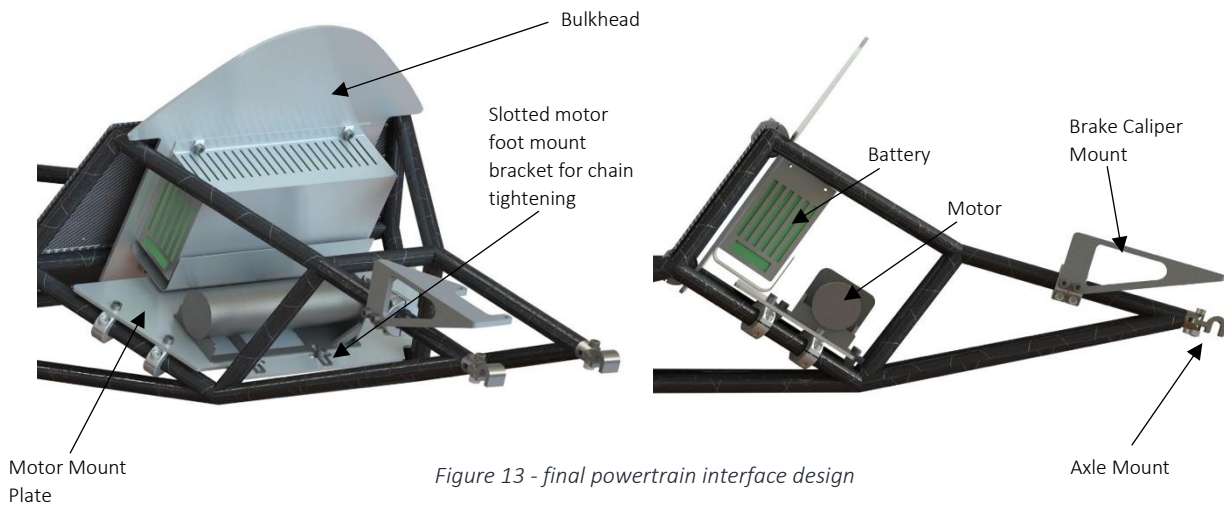


Figure 13 - final powertrain interface design

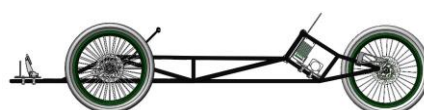
Anthropometrics and Ergonomics

A significant proportion of road accidents are the result of driver fatigue; with the severity of injuries also influenced by the ride position of the victims in the vehicle. Fatigue was particularly relevant in this case, given the tight space constraints and the length of the race with an estimated driving time of one hour. In order to reduce risks, vehicle ergonomics had to be considered with a view to promote ride comfort, reducing fatigue, whilst considering the driver’s spatial consciousness (Kovacevic, 2010).

As outlined in the PDS, the requirement was for the vehicle to hold a 5’ 5” female driver whose dimensions were examined. The following results were found (Kovacevic, 2010).

Table 16 – 5’ 5” female driver dimensions

Dimension Name	Length (mm)
Buttock height	854
Buttock-knee length	600
Elbow rest height - standing	1014



Elbow centre of grip length	335
Eye height – sitting	741
Forearm breadth	480
Functional leg length – seated	1030
Hip breadth	350
Shoulder height - standing	1354
Height	865
Height stature	165

Incorporation into the Design

With the measurements found through research, a scaled design was produced for the lateral cross section of the vehicle (Figure 14). The design was developed around the requirement of the driver’s knees having to be in line with the front wheel axles. This was necessary to ensure the drivers legs did not interfere with the steering system. The design also incorporated the 150 mm ride height to enhance aerodynamic performance (set by the Aerodynamic Lead of the project) and the general dimensional decisions described in the ‘Wheelbase and Track Width’ section.

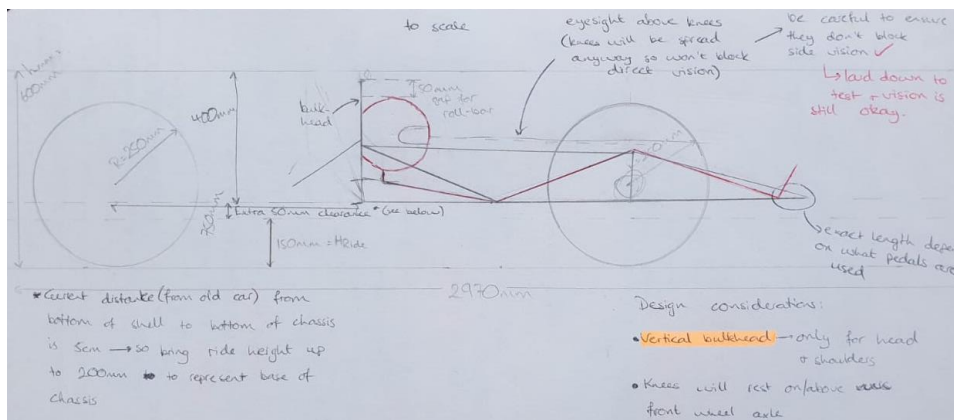
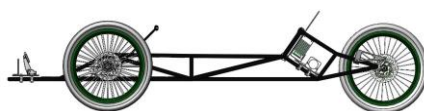


Figure 14 -phase 1 lateral dimensions schematic

With the foundation for the design set, the initial design was iterated to integrate the powertrain interface, accommodate the pedal box, increase the triangulation of members for better stress distribution and to ensure that the chassis would fit in the shell as shown in Figure 15



Figure 15 - design iterations



The anthropometric data of Table 16 was then reconsidered to develop the resulting design (Figure 16), adjusting the length of relevant sections so that the driver’s body parts could sit in the locations indicated to ensure that the main loads of the driver’s weight were at nodes.

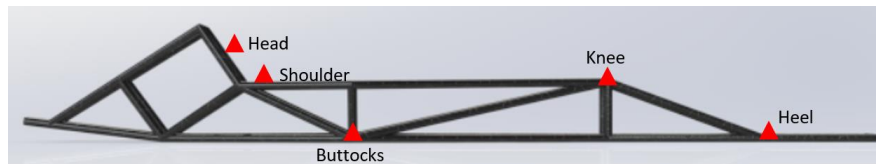


Figure 16 - anthropometric considerations

Final Chassis Design

The final chassis layout is shown in Figure 17, with numbers labelling each node. Note that this labelling scheme is used throughout the ‘Validation of Design’ section. This final design incorporates the considerations of ease of manufacture, strength, weight, ergonomics, shell fit and compatibility with powertrain components.

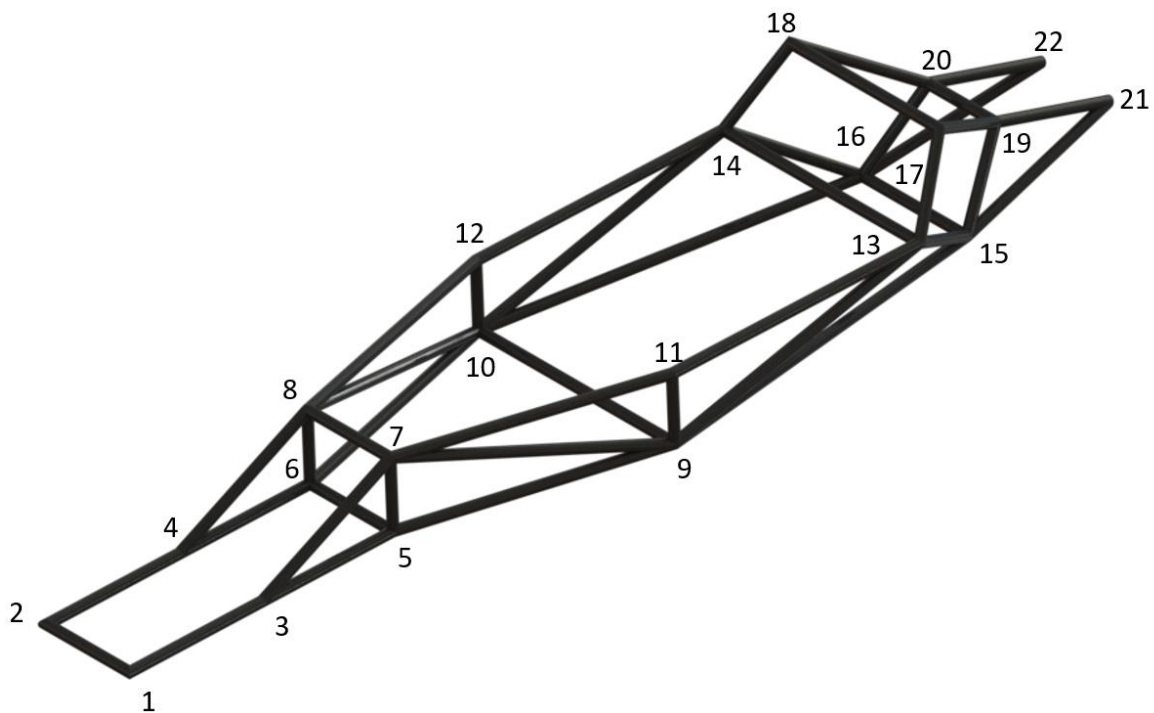


Figure 17 - final spaceframe with nodal annotations

Validation of Design

Modes of Deflection for Automotive Chassis

A structurally stable chassis would have to mitigate against the typical automobile deflection modes summarised in Table 17.

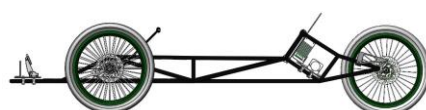
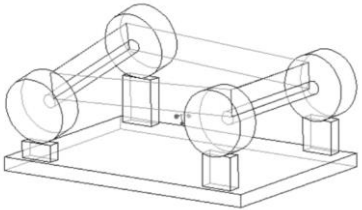
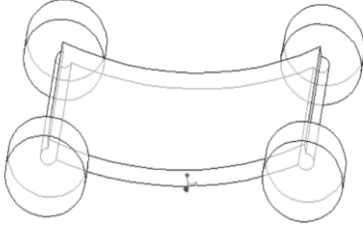
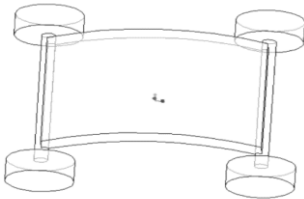
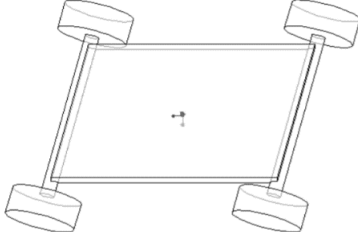


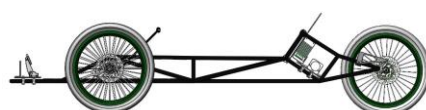
Table 17 - failure modes

Mode	Description
<p data-bbox="183 259 408 288">Longitudinal Torsion</p> 	<p data-bbox="807 259 1412 450">Results from an imbalance of forces on opposite corners of the vehicle. It is experienced at every corner of a track due to the lateral weight transfer that occurs when cornering. During this loading case, the chassis can be modelled as a torsional spring that connects the two corners where the loads act.</p>
<p data-bbox="183 589 363 618">Vertical Bending</p> 	<p data-bbox="807 589 1412 846">Results from any vertical loads, including those induced from vertical acceleration, acting on the structure, with the main contribution coming from the weight of the driver. The reaction to these forces is distributed across the axles, where contact with the floor is made through the tyres. In this loading case, the frame can be modelled as a simply supported beam – see ‘Simply Supported Beam Model of Chassis’.</p>
<p data-bbox="183 1023 355 1052">Lateral Bending</p> 	<p data-bbox="807 1023 1412 1182">Similar to longitudinal torsion, the main cause of these loads is due to centrifugal forces when cornering. Side winds and the road camber can also cause lateral bending. These lateral forces are resisted by friction between the tyres and the road, causing bending.</p>
<p data-bbox="183 1305 416 1335">Horizontal Lozenging</p> 	<p data-bbox="807 1305 1412 1464">Horizontal lozenging occurs as a result of forward and backward forces that are applied at opposite wheels. These forces are due to the continuous impact of the wheels with potholes, curbs, and general vertical variations in the road.</p>

Generally, if the torsional stiffness and vertical bending stiffness are satisfactory, then the resistance to lateral bending and horizontal lozenging will also be sufficient (Singh, 2010). The following sections therefore focus on vertical bending and longitudinal torsion as well as stresses in individual members.

Spaceframe Deflections and Stresses

It was important to find the amount of vertical deflection in the spaceframe due to applied forces as excessive deflection would potentially have an adverse effect on the ride height, driver ergonomics, chain alignment and steering system angles. If the spaceframe deflection exceeded the 0.5 m



clearance gap between the chassis and shell, abrasion of tubes and the shell interior may result as they rub. When designing the spaceframe, a simply supported beam model was used to find the deflection in either side section of the spaceframe, with the wheels representing simple supports. It was reasoned that, should the deflections be acceptable in this oversimplified model, the deflection of the actual chassis would certainly be acceptable as its truss structure is known to have better deflection behaviour than a beam (Lin, 2017). This was verified by finding more accurate deflection values by applying an energy method for a truss structure.

Given that the tubes can be modelled as being pin-jointed to each other, the only loads that will be experienced by the majority of the tubes will be axial tension and compression. This is a benefit due to the very strong tensile and compressive load carrying capacity of the carbon fibre tubes chosen.

Loading Condition

In its static loading condition, the chassis is subject to the weight of the driver, the weight of the pedal box and the weight of the powertrain components. The Powertrain DMT team estimated the pedal box and powertrain components to be 10 kg each, and the driver mass that the vehicle had been designed for was 60 kg. The centre of mass of a person on average lies between their stomach and chest (Grabarczyk, 2003). The centre of mass of the driver was therefore modelled as lying between nodes 9/10 and 13/14. As shown in Figure 18, this was considered along with the approximate locations of the pedal box and powertrain centre of masses to calculate a total centre of mass location of 1.2 m from the front most member of the spaceframe and 0.65 m from the front wheels.

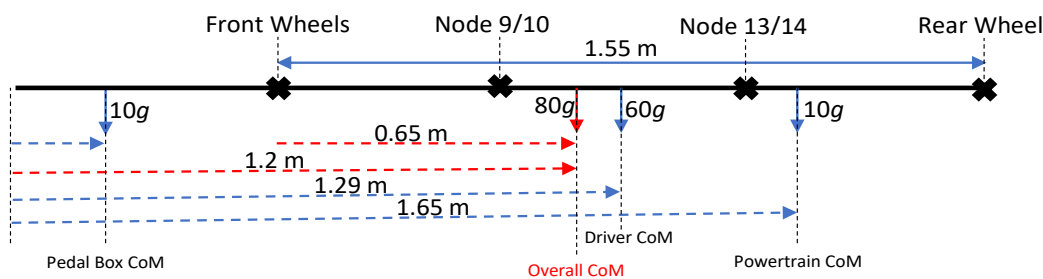
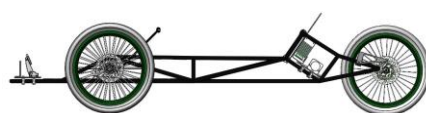


Figure 18 - determining centre of mass

The dynamic loading conditions are more difficult to estimate as they will be determined by shock loads from bumps in the road. In literature, this is accounted for by applying a dynamic multiplication factor to all loads (Seward, 2014). For the simply supported beam model, this was neglected since the purpose of this model was not to give an accurate representation of the deflections, but to provide a qualitative verification of their acceptability in the actual case. For the all other stress and deflection analysis, a dynamic multiplication factor of 1.2 has been used. This is a relatively low dynamic multiplication factor but is suitable for the purposes of this vehicle since the Shell Eco-Marathon racetrack is a smooth professional racetrack and the vehicle will be travelling at a low maximum



speed of 8 ms^{-1} (Simmons, 2019). The dynamic loading conditions would also involve centripetal loads translated to the chassis, causing torsional stresses that have been modelled using FEA.

Simply Supported Beam Model of Chassis

As shown in Figure 19 below, the simply supported beam was modelled as being subject to a centrally applied load of $40g$ since the location of the true centre of mass was approximately halfway between the wheels as seen in Figure 18. Modelling the load as $40g$ assumes that the total load would be split equally between either of the side sections. In reality, some load would be taken by the transverse

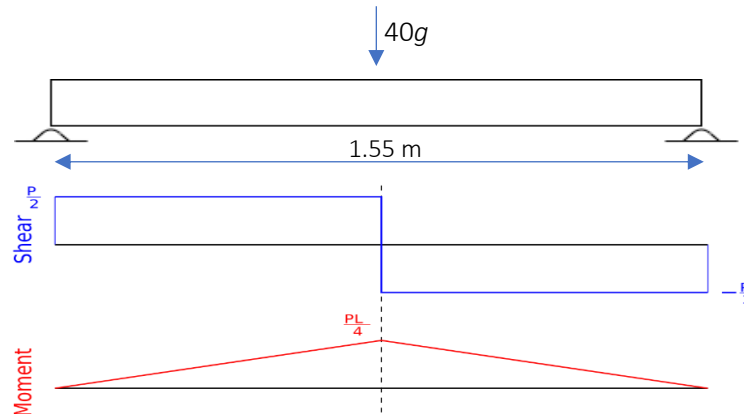


Figure 19 - shear force and bending moment diagrams for simplified model

spaceframe members joining the two side sections, making this a conservative estimate. In this loading case, the shear force diagram and bending moment diagrams are as shown.

The maximum bending moment is therefore at the location of the centrally applied load and equal to $PL/4$. This value can be used to find the maximum stress experienced by the beam using Equation 6.

$$\sigma = \frac{My}{I} \tag{6}$$

Should the beam in this model be treated as a single carbon fibre tube of outer diameter 20 mm and inner diameter 18 mm, the second moment of area would be $2.7 \times 10^{-9} \text{ m}^4$. Applying this to Equation 6 under the maximum bending moment condition, the stress is found to be 563.2 MPa, which exceeds the tube yield stress of 153.6 MPa found from testing. Considering the spaceframe's structure (Figure 17) it was identified that, at the location halfway between the wheels, the spaceframe's side section is comprised of three members. The second moment of area was therefore recalculated using the parallel axis theorem (Equation 7), with the beam modelled as three carbon fibre tubes stacked vertically (Figure 20).

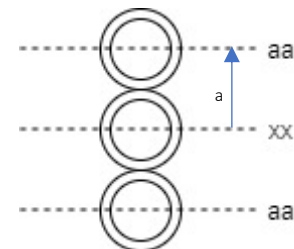
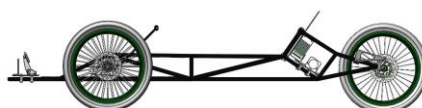


Figure 20 – structure cross-section

$$I_{xx} = \Sigma(I_{aa} + a^2A) \tag{7}$$



The adjusted second moment of area was $5.59 \times 10^{-8} \text{ m}^4$. When this was applied to Equation 6, the maximum stress was found to be 27.2 MPa which is less than the yield stress of either the plain carbon fibre tube (153.5 MPa) or the carbon fibre tube with a joint in it (71.8 MPa). This model could therefore be used to find the deflection in the spaceframe side section using Equation 8. This relation was derived by taking the deflection-moment relation and applying boundary conditions of zero deflection and zero moment at the simple supports.

$$\delta = \frac{WL^3}{48EI} \tag{8}$$

The Young’s Modulus of the beam model was calculated to account for the fact that the spaceframe side section contained several joints between the front and rear wheels. These joined tube sections have a Young’s Modulus of 734.3 MPa whereas the plain tube section would have a Young’s Modulus of 23.8 GPa. Since the stress in bending is along the length of the beam, the composite of plain and joined sections can be modelled as shown in Figure 21.

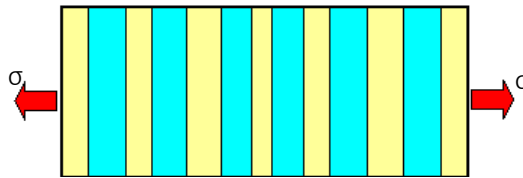


Figure 21 – material model for beam

For this case, the Young’s Modulus can be found as in Equation 9, where v_{js} is the volume ratio of the joint sections and E_{js} and E_{pt} are the respective Young’s Moduli of the joint section and plain tube.

$$E = \frac{1}{\frac{v_{js}}{E_{js}} + \frac{1 - v_{js}}{E_{pt}}} \tag{9}$$

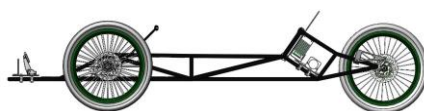
Since there are 9 joints between the front and rear wheel locations at nodes 5/6 and 21/22 respectively as seen in Figure 17, the volume ratio of the joint sections can be found as shown, where all joints are modelled as 30 mm long sections.

Plane Tube Length: Joint Section Length

$$(1550 - 9 \times 30) : (9 \times 30)$$

$$1280 : 270$$

This gives a v_{js} value of 0.174. Inserting this into Equation 9 gives a total Young’s Modulus of 3.68 GPa. Applying this to Equation 8 gives a side section deflection of 0.15 m. Though this is a significant deflection, it is less than the clearance gap between the chassis and shell of 0.5 m and since this simply supported beam model is a gross simplification of the real situation, the true deflection would



be acceptably small. A truer representation of the deflection experienced was estimated by applying energy methods and treating the structure as a pin-jointed frame.

Pin-jointed Frame Model and Energy Method (AWP)

This method involved treating the spaceframe side section as a pin-jointed frame simply supported at the wheel locations (Figure 22) and finding the tensions in each member before applying Castigliano’s theorem to find the deflection at a node where a force is applied (Equation 10).

$$\delta_j = \frac{\partial U}{\partial W_j} = \sum_{i=1}^N \frac{T_i L_i}{E_i A_i} \frac{\partial T_i}{\partial W_j} \tag{10}$$

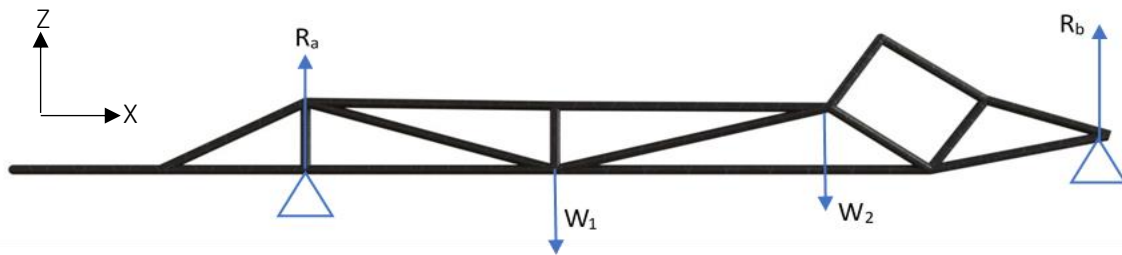


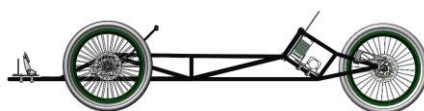
Figure 22 - pin-jointed, simply supported model

To make it possible to find all the tensions in the spaceframe section, the transverse angles of its members were ignored and it was instead treated as a flat truss structure, with member lengths equal to the projection of the member lengths in the X-Z plane as found from the CAD model. The energy method required that loads be applied at nodes. The total side section load of 40g was therefore modelled as equivalent loads W₁ and W₂ at nodes 9/10 and 13/14 – the nodes adjacent to the centre of mass location – as shown in Figure 18.

Tensions were first found for each member using the method of sectioning and applying equilibrium to the whole structure as well as individual nodes. The contribution of each member to the deflections at nodes 9/10 and 13/14 were then found in terms on W₁ and W₂ using Equation 10. Table 18 below summarises these results. The Young’s Modulus value used was simply that for a plain tube, 23.8 GPa, and the area of the tube cross section was calculated to be 5.97 x 10⁻⁵ m².

Table 18 - deflection contributions of spaceframe members

Member	Tension	$\frac{\partial T}{\partial W_1}$	$\frac{\partial T}{\partial W_2}$	L (mm)	$\frac{TL}{EA} \frac{\partial T}{\partial W_1} (\times 10^{-8})$	$\frac{TL}{EA} \frac{\partial T}{\partial W_2} (\times 10^{-8})$
1-5 / 2-6	0	0	0	556	0	0
3-7 / 4-8	0	0	0	308	0	0
5-7 / 6-8	-0.69W ₁ -0.35W ₂	-0.69	-0.35	137	4.59W ₁ +2.33W ₂	2.33W ₁ +1.18W ₂
7-11 / 8-12	-2.52W ₁ -1.28W ₂	-2.52	-1.28	475	212W ₁ +108W ₂	108W ₁ +54.8W ₂
7-9 / 8-10	2.61W ₁ +1.33W ₂	2.61	1.33	492	236W ₁ +120W ₂	120W ₁ +61.3W ₂
5-9 / 6-10	0	0	0	475	0	0
9-11 / 10-12	W ₁	1	0	130	9.15W ₁	0
11-13 / 12-14	-2.52W ₁ -1.28W ₂	-2.52	-1.28	522	233W ₁ +119W ₂	119W ₁ +60.2W ₂
9-13 / 10-14	1.28W ₁ -1.45W ₂	1.28	-1.45	538	60.2W ₁ -70.3W ₂	-70.3W ₁ +79.6W ₂
9-15 / 10-16	1.28W ₁ +2.69W ₂	1.28	2.69	713	82.2W ₁ +173W ₂	173W ₁ +363W ₂
13-15 / 14-16	-1.24W ₁ -2.60W ₂	-1.24	-2.6	229	24.8W ₁ +52.0W ₂	52.0W ₁ +109W ₂
13-17 / 14-18	-0.45W ₁ -0.95W ₂	-0.45	-0.95	171	2.44W ₁ +5.15W ₂	5.15W ₁ +10.9W ₂



17-19 / 18-20	$-0.61W_1-1.29W_2$	-0.61	-1.29	235	$6.15W_1+13.0W_2$	$13.0W_1+27.5W_2$
15-19 / 16-20	$-0.19W_1-0.38W_2$	-0.19	-0.38	177	$0.45W_1+0.90W_2$	$0.90W_1+1.80W_2$
19-21 / 20-22	$-0.67W_1-1.38W_2$	-0.67	-1.38	248	$7.84W_1+16.1W_2$	$16.1W_1+33.2W_2$
15-21 / 16-22	$0.65W_1+1.35W_2$	0.65	1.35	350	$10.4W_1+21.6W_2$	$21.6W_1+44.9W_2$

Summing the sixth and seventh columns gave the deflection at node 9/10 and node 13/14 respectively. The expressions for each of these deflections are shown in Table 19. It was calculated by a moment balance that the 40g load at the centre of mass position could be represented as a W_1 load of 27.1g and a W_2 load of 12.9g. Multiplying each of these values by 1.2, the dynamic load factor, gave a W_1 load of 32.5g and a W_2 load of 15.5g. Applying these to the expressions for each of the deflections gave the deflection values shown in Table 19.

Table 19 - deflections found from Castigliano's theorem

Node	Deflection Expression ($\times 10^{-6}$)	Deflection (mm)
9/10	$8.89W_1 + 5.61W_2$	3.69
13/14	$5.61W_1 + 8.47W_2$	3.08

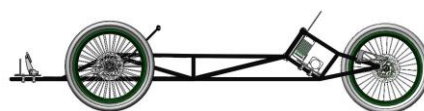
These deflection values vary from that found using the oversimplified simply supported beam model, 0.15 m, by two orders of magnitude. This proves the extent of the beam model simplification, showing that it was certainly a suitable model to justify the acceptability of the actual deflections.

Applying the W_1 and W_2 values to the tension expressions found in Table 18, the greatest tension is found to be 1034.4 N in member 7-9 / 8-10. This corresponds to a stress of 17.3 MPa, which is less than the yield stress of either a plain or joined tube. This validates that no tube member will yield.

The longest spaceframe member is 9-15 / 10-16 which is 713 mm. Since the Euler buckling load is inversely proportional to the square of the member length as shown in Equation 11, this member was used to find a compressive load buckling limit of 1247.6 N, which offers a conservative limit for all other tube members. The greatest compressive load in the spaceframe is found to be 864.6 N in members 7-11 / 8-12 and 11-13 / 12-14. This validates that no tube member will buckle.

$$P_E = \frac{\pi^2 EI}{L^2} \tag{11}$$

It should be noted that this pin jointed model is also a simplification. The lugs and significant layers of wet layup wrapping at each of the joints may make them more restrictive than a pin joint model would imply, with restrictive moments potentially being present. This would suggest that the deflection values found are an overestimate. However, the Young's Modulus values in the region of the joints would be lower than the plain tube value. This has not been accounted for in the calculation of the deflections and would suggest that these deflection values are therefore an underestimate. Another significant simplification is the modelling of all the loads experienced by the spaceframe section as point-loads at two nodes. The fact that some of the side section spaceframe's members are



angled in the transverse direction could also be considered when finding the tensions in each of the members to find more accurate deflection values. The qualitative effect of this simplification is not easily discernible. In a typical case, an FEA model could be used to find more accurate deflection values and verify the hand calculations. However, this would require an exact model of the way in which the material behaves. Since the carbon fibre material of the tubes and carbon wrapping results in variable material properties and behaviours, such an FEA would offer deflection values that are no more accurate than those found with this energy method. Nevertheless, member stresses found in the 'FEA Corroboration' section highlight discrepancies due to the simplifications of this model.

Maximum Bending Stress in the Carbon Fibre Tubes

Even though the chassis could be modelled as a pin-jointed frame, some tubes will inevitably be loaded in bending, mainly the tube connecting nodes 9 and 10 as well as the tube connecting nodes 13 and 14 together. These tubes are located directly under the driver's body and so they will be expected to be exposed to the greatest bending loads. From these two tubes, the most critical one will be the tube connecting nodes 9 and 10 together as it will carry the load exerted by the driver's back (on the floor panel behind this tube) as well as the driver's bottom (on the floor panel ahead of this tube). These loads are expected to account for approximately two thirds of the driver's weight, or approximately 40 kg. However, it is important to note that the floor panels will be supported along all four edges which means that this tube will only experience one quarter of this expected load, resulting in approximately 10 kg of load on this tube. This was increased to 12 kg (or 117.72 N) for the purposes of the stress analysis calculations, to account for the 1.2 dynamic multiplication factor.

This load will be distributed along the length of the tube as the panels will be attached to the tubes using cable ties at regular intervals. The presence of internal lugs as well as extensive exterior wet lay-up bonding at each end of the tube was more accurately modelled as built-in end conditions, resulting in the bending moment diagram shown in

Figure 23. The bending moment is expressed in terms of w which is the magnitude of the distributed load per metre (in this case 261.6 Nm^{-1}) and L which is the length of the tube (in this case 450 mm).

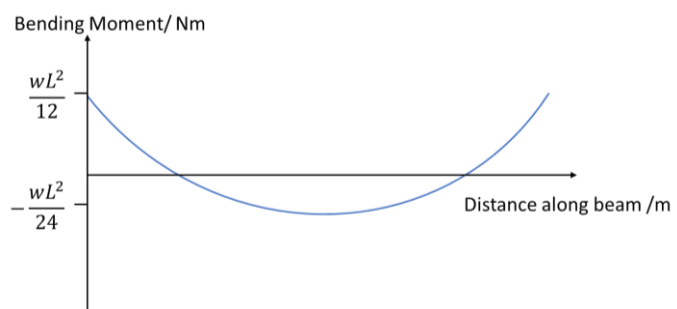
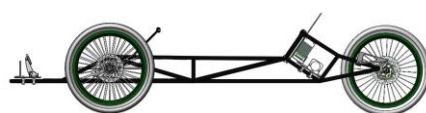


Figure 23 – bending moment diagram for pin-jointed, simply supported model

Applying the central bending moment to

Equation 6, it was possible to determine that the maximum bending stress acting at the centre of the



tube's length would be 8.17 MPa. This is significantly lower than the failure stress of the tubes obtained from the testing phase of 153.6 MPa.

Maximum Bending Stress at the Nodes

It was also important to determine the maximum stresses acting at the nodes to ensure that the wet lay-up bonding of the tubes would be strong enough for this application. The tube connecting nodes 9 and 10 was also used for this analysis.

In this scenario, the largest bending moments would occur at the built-in ends, as shown in Figure 23 above, which could be expressed as $\frac{wL^2}{12}$. This results in a bending moment of 4.41 Nm acting at each node of this tube.

Each layer of cured carbon fibre lay-up was estimated to have a thickness of 0.3 mm. It was also estimated from prototype testing that a minimum of four layers would be required per joint. Therefore, the geometry of the joint was approximated as a cylinder, with internal diameter equal to the external diameter of the tubes (20 mm) and external diameter of 22.4 mm given by the four layers of wrapping. Using Equation 6, the bending stress at the joints was estimated as follows:

$$\sigma = \frac{4.41 \times 0.0112}{\left(\frac{\pi(0.0112^4 - 0.01^4)}{4}\right)} = 11 \text{ MPa}$$

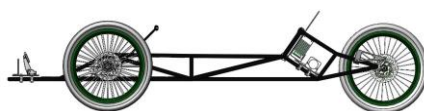
This value obtained was significantly less than the failure stress of the carbon fibre joints which was found to be 71.8 MPa through testing.

Finite Element Analysis Corroboration of Chassis Design (AWP)

Finite Element Analysis (FEA) tools could be used to obtain a general idea of the distribution of stresses across the different chassis members during normal operating conditions.

However, there are major limitations to how informative these results would be:

- Results are only useful if they could be validated through the use of simpler hand calculations or experiments.
- Strains and deflections require an exact model of the way in which a material behaves and mechanical property descriptors such as Young's modulus and Poisson's ratio. These cannot be accurately determined for the carbon fibre materials used in this project.



The material choice has little effect on the stresses obtained through these software tools as these values depend on the chassis geometry and loading conditions. Deflection results, however, would not be accurate. For the purposes of this analysis, the tube material was set to aluminium 6063-T6 as this was observed to result in accurate stress values of simpler models compared to hand calculations.

A 3D model of the chassis was entered into the software to create a mesh where loads and fixed geometry could be applied, as shown in Figure 24. Using the same joint numbering system as in Figure 17, nodes 5, 6, 21 and 22 were selected as immovable points to model them as pin supports which accurately approximates the behaviour of the wheel bearings at those locations.

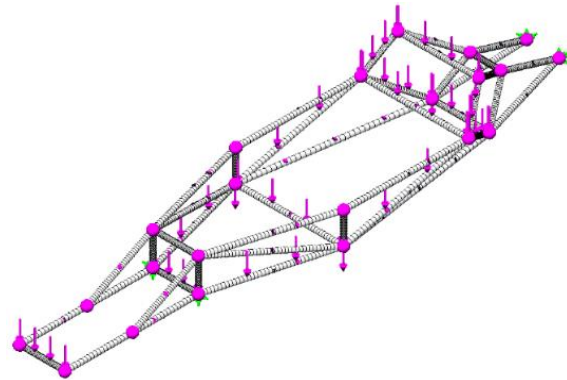


Figure 24 – vertical loads applied to chassis during FEA analysis

The weight of the tubes was considered negligible for this analysis compared to the magnitudes of the applied loads as summarised in the ‘Loading Condition’ section. A dynamic multiplication factor of 1.2 was applied to all loads. These were then distributed along the corresponding tubes as shown in Table 20. The result of the analysis is shown in Figure 25.

Table 20 - vertical loads applied

Load applied vertically downwards (N)	Tube
117.72	1-2, 9-10
58.86	5-9, 6-10, 5-6, 9-13, 10-14, 13-14
39.24	17-18, 13-17, 14-18
78.48	15-16, 14-16, 13-15

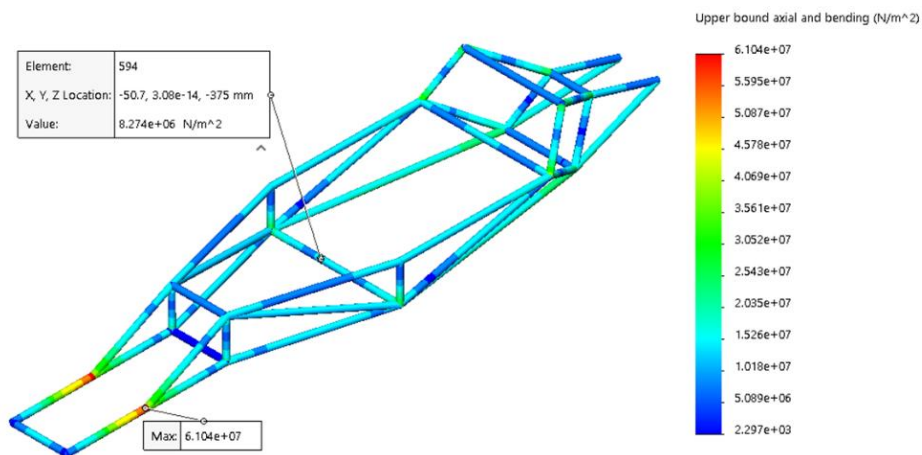
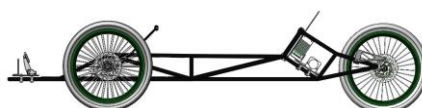


Figure 25 – vertical loading FEA analysis results



An important result is the stress obtained at the centre of the tube joining nodes 9 and 10. As shown in Figure 25, this tube exhibited a stress of 8.27 MPa at its centre which is very similar to the value obtained using hand calculation shown previously of 8.17 MPa. Similarly, higher stress can be observed in the contour plot at the ends of this tube, corresponding to the location of the carbon fibre wet lay-up joints. This agrees with the assumption stated previously suggesting that these joints may behave as built-in instead of pin-jointed.

Overall, the stresses exerted on the chassis are very low, on average having a value in the range of 10 to 20 MPa, as observed in Figure 25. These values are significantly lower than the failure stresses obtained through testing, suggesting that this design could successfully withstand the loads expected during the Shell Eco-marathon competition. Nonetheless, there are regions where higher stresses are observed in the results of this analysis. The maximum stress was determined to be 61.0 MPa acting on nodes 3 and 4. This value, while below the failure stress of the joints, was still considerable which led to particular care being taken in the wrapping process of these particular joints, to extract the maximum available strength from the carbon lay-up material.

A similar study was carried out to investigate the stresses generated by the torsional deflection of the chassis due to the lateral cornering forces generated at the track. As mentioned in the 'Steering Design' section of this report, the maximum lateral force that could be generated at each wheel was 324 N. This results in a maximum lateral force of 648 N for the two front wheels which, in turn, corresponds to a total moment of 164.6 Nm acting on the plane of the front wheels (approximated by the plane made up by the nodes 5, 6, 7 and 8). This load was applied to the mesh generated previously and the results obtained are shown in Figure 26.

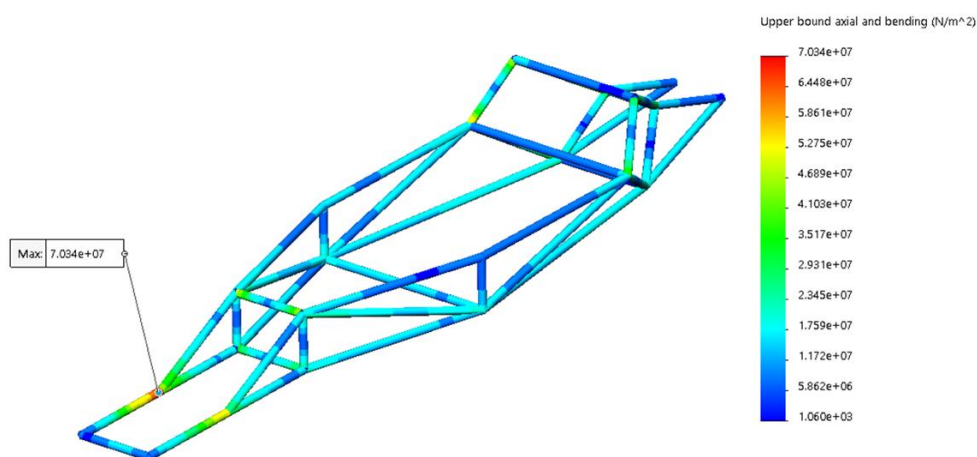
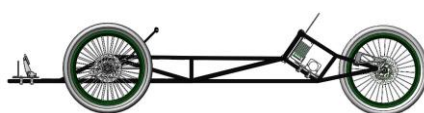


Figure 26 – torsional FEA analysis results

These results suggest that the maximum stress acting on the chassis would increase, as expected. The maximum stress was now found to be 70.3 MPa on joint 4 which is also below the critical failure



stress of the joints. Nonetheless, it is still considerably high. However, it is important to note that this loading condition corresponds to the worst-case scenario in which the tyres are at their limit of traction with the road. This is equivalent to the vehicle travelling at a speed of 8 ms^{-1} through a corner of radius 8 m, which is very unrealistic according to discussions with the Powertrain DMT. Nevertheless, every effort was made during the manufacturing plan to ensure that there would be additional carbon fibre material applied at these critical locations during the wet layup process.

Manufacturing of Spaceframe

Chassis Assembly

In total the spaceframe consisted of 38 tubes components, total length of 14.06 m, and 18 lugged inserts. The 15 easy composites ltd 1 m carbon fibre tubes were marked up and labelled using a ruler and tape ready for cutting. The lugged inserts were hollow, solid, plastic parts 3D printed in the Imperial College Advanced Hackspace.



Figure 27 – chassis alignment using internal lugs

Tubes were cut in the pit garage, using a hacksaw with the extractor fan to collect dust produced immediately. Masks, goggles, lab coats and gloves were worn to mitigate the health hazards as outlined in the risk assessments. Once the tubes were cut and it was identified which tubes connected to which lugs, the surfaces of the lugs were filed down to slot into tubes easily. The majority of the tubes slot on easily, however additional cuts were made where a tube required an extreme angle to fit onto a lug. The assembled spaceframe is shown in Figure 27.

Final Layup Process

The process outlined here is an optimised and sophisticated layup constructed after multiple prototype joints were produced and tested. Firstly, the surfaces of all tubes within 5 cm from joints were filed using sandpaper while wetted and then cleaned with acetone to increase the surface adhesion and maximise the strength of the cured layup. The Easy Composites Ltd EL2 resin and hardener was weighed and mixed in a ratio of 10:3 and steps 1 to 5 below were repeated for all joints and left to cure for 24 hours.

1. Cut a strip of weave around 0.5 m long and paint fully with the resin hardener mixture.
2. Begin wrapping around each tube member tightly and slowly, moving in a longitudinal direction (Figure 28), covering at least 30 mm of each exposed tube and ensuring the fibres are kept straight and prevented from fraying.

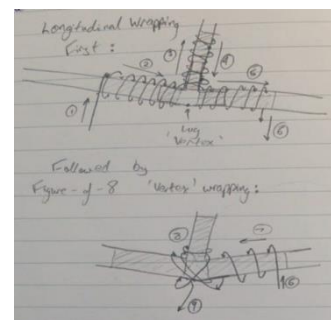
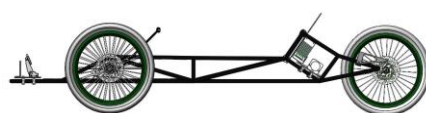


Figure 28 – wrapping motion of weave



3. Wrap a coated strip of narrow weave around the vertex centre itself by using a figure of eight motion.
4. Repeat steps two and three until a minimum of 3 layers are applied around the joint.
5. Cover in the composite shrink tape (Figure 29) and apply heat gun gently at a distance of 20 cm for 5 seconds to shrink the tape without breaking it.

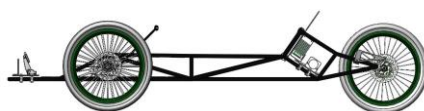


Figure 29 – use of shrink tape during manufacture



Figure 30 – new carbon fibre chassis (left) vs old steel chassis (right)

Figure 30 above shows the new carbon fibre spaceframe side by side with the previous entry chassis. The new spaceframe weight was 2.25 kg, compared to the previous entry chassis weighing 9.65 kg. With steering system and powertrain interface components, the floor panels and the bulkhead fitted, the chassis was 5.6 kg, and therefore still met the target set in the PDS of being at least 10% lighter than the previous entry.



POWERTRAIN INTERFACES

Motor Mounting

The motor mount plate is shown in Figure 31. Where the motor foot mount bracket has longitudinal slots that allow the motor position to be adjusted to tighten the chain before bolting, the mount plate has slots in the transverse direction to allow for adjustment to correct chain misalignment.

A concern with the motor mount plate was its potential to begin vibrating in resonance if a periodic force due to a mass out-of-balance in the motor excites the plate's natural frequency. This could potentially damage the rear spaceframe or the chain. The natural frequency of the plate was investigated by modelling the plate as rectangular, with a length of 355 mm (its average length) and a width of 168 mm. Since the plate was to be bolted to the rear chassis members along its left and right edges via collar pieces, with its top and bottom edges left free, the situation was modelled as in Figure 32, giving the following boundary conditions, where Z is the displacement function.

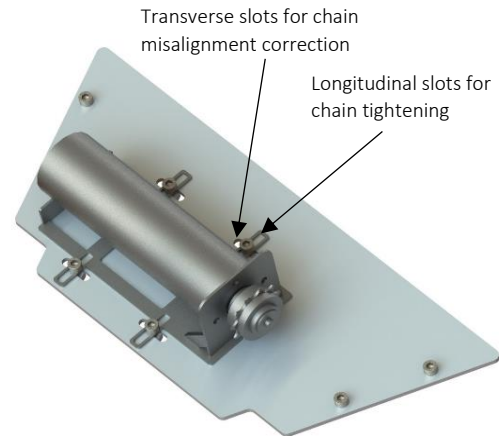


Figure 31 – final motor mounting design

1. $Z = 0$ along AC and BD
2. $\frac{\partial Z}{\partial x} = 0$ along AC and BD
3. $M_y = -D \left[\frac{\partial^2 Z}{\partial y^2} + \nu \frac{\partial^2 Z}{\partial x^2} \right] = 0$ along AB and CD

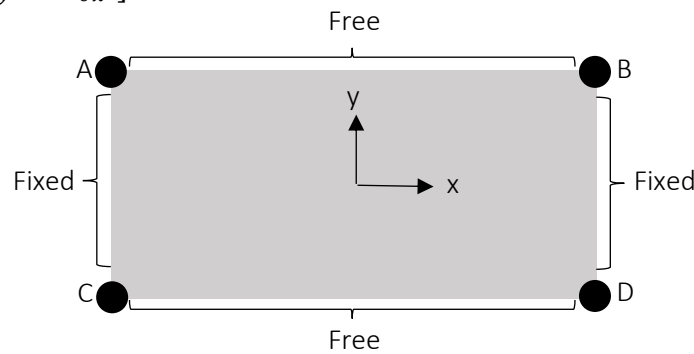
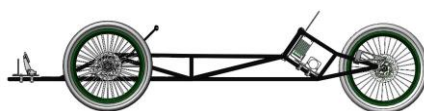


Figure 32 – motor plate model for vibration analysis

Applying these boundary conditions to the general form of the displacement function in a rectangular plate, shown in Equation 12, gives the result for the natural frequency shown in Equation 13 (Steinberg, 2000). The plate stiffness D is calculated as in Equation 14.

$$D \left[\frac{\partial^4 Z}{\partial x^4} + 2 \frac{\partial^4 Z}{\partial x^2 \partial y^2} + \frac{\partial^4 Z}{\partial y^4} \right] + \rho h \frac{\partial^2 Z}{\partial t^2} = 0 \quad (12)$$



$$f_n \approx \frac{3.55}{b^2} \sqrt{\frac{D}{r}} \tag{13}$$

$$D = \frac{Eh^3}{12(1 - \nu^2)} \tag{14}$$

Applying the relevant material properties of aluminium with a plate thickness value, h , of 4 mm and a free edge length, b , of 410 mm gives a natural frequency of 8.14 Hz or 488.4 rpm. This is less than the motor running speed of approximately 5730 rpm as confirmed with the Powertrain DMT team, therefore proving the motor mount design to be safe.

Axle Mount Component

The rear axle was to be 135 mm in length, with 30 mm long 10 mm diameter threaded sections extending from its ends. To mount the axle, a pair of tube-hook components as in Figure 33 were conceptualised.

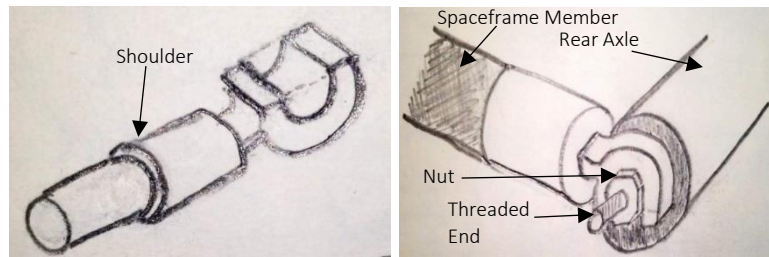


Figure 33 – initial axle mounting concept

At one end, the component would slot into the spaceframe’s rear-most members, with its shoulder sitting against the end, and methacrylate adhesive would be applied to keep it in place (VM100 Black as recommended by Easy Composites). On the other end, a hook would sit on the threaded axle ends and a nut would be tightened against the outer face to secure the axle.

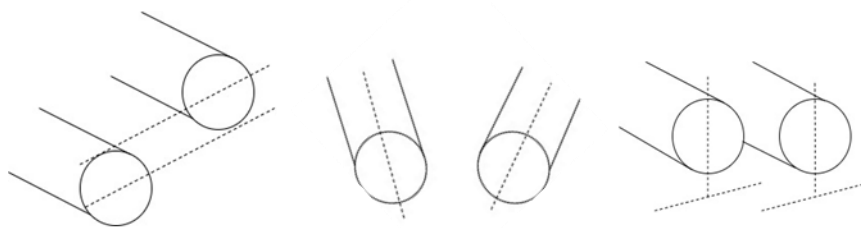
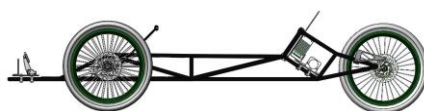


Figure 34- vertical, angular, and longitudinal misalignment respectively

Potential misalignments of the spaceframe’s rearmost members due to inaccuracy in the tube joining and assembly method are shown in Figure 34. The conceptualised axle mount components would be able to overcome vertical or longitudinal misalignment by the relative adjustments shown in Figure 35.



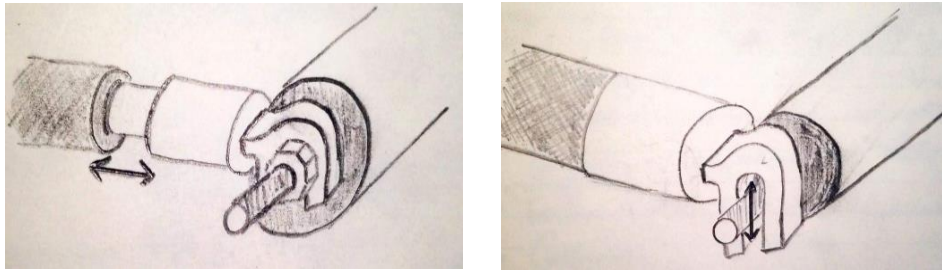
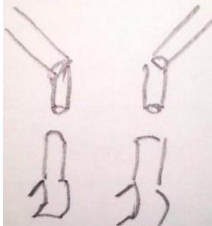
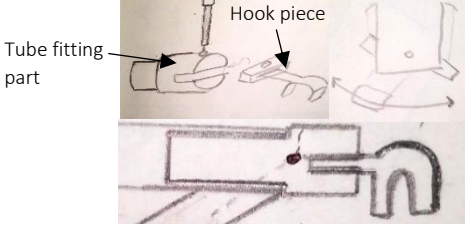


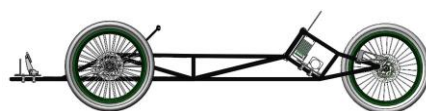
Figure 35- Adjustment methods to correct for longitudinal and vertical misalignment respectively

To overcome longitudinal misalignment, the axle mount component on the side for which the rear spaceframe member is relatively short would be extended out of the tube by an appropriate amount before methacrylate adhesive is applied (such that the tube end would no longer sit against the shoulder). To overcome vertical misalignment, the hook part of the components would be made long enough such that the nut could still be tightened against its outer face without the hook having to sit flush with the threaded end.

Nevertheless, the conceptualised axle mount component could not be adjusted to overcome angular misalignment that might occur. Table 21 therefore summarises two considered adjustments to the axle mounting method to mitigate against angular misalignment and their relative merits.

Table 21 - mounting axle component adjustment options

Proposed Adjustment	Addition of short, straightening spaceframe members.	Component made in two parts – a tube fitting part that bolts to a hook piece.
Explanation	Once the spaceframe is assembled, short members would be joined to the rear-most spaceframe members, ensuring that they are straight and parallel.	Each of the hook pieces can be slotted into the tube fitting parts and bolted at appropriate angles such that the hook pieces are straight and parallel.
Sketches		
Pros	<ul style="list-style-type: none"> - Vertical and longitudinal misalignment mitigation methods proposed in Figure 35 can still be employed. - Also offers extra mitigation against longitudinal misalignment through length of straightening members. This would be useful in case this misalignment is so significant that extension of the component out of the tube as in Figure 35 is insufficient. 	<ul style="list-style-type: none"> - Vertical and longitudinal misalignment mitigation methods proposed in Figure 35 can still be employed. - Easily adjustable to mitigate angular misalignment completely.
Cons	<ul style="list-style-type: none"> - Since the angle of the joints that need to be made would be dependent on the observed angular misalignment and not on the intended design, creating the lugs required for these joints would prove challenging. 	<ul style="list-style-type: none"> - It would be preferred for the axle mount components to be manufactured using CNC to maintain accuracy and symmetry between each of the pair. Splitting the component into two will mean that the axle mounts will account for four CNC requests



	<ul style="list-style-type: none"> - The joining of these short members may lead to misalignments just the same as any other joint in the spaceframe, which was the cause for misalignment concerns in the first place. However, since the misalignment is now dependant on only this joint, the likelihood is lower as misalignment wouldn't aggregate across all the spaceframe joints. - The region near the axle mount would experience the reaction force of the rear wheel as well as shock forces. Therefore, the shortness of the tube member and the weakening effect of the joint may result in yielding stresses here. - The rear-most point in the spaceframe was designed to be a node to improve the stress distribution. Adding these short members would therefore negate this consideration, worsening the stress distribution as the forces experienced at the axle mounts are cantilever loads. 	<p>rather than two. Since several steering system components also had to be made by CNC milling, this would likely mean that some of these axle mount CNC requests are rejected, meaning parts would have to be manufactured by hand. This is potentially a source of inaccuracy and asymmetry, which itself has the potential to result in misalignment.</p>
--	---	---

It was reasoned that the adjustment of the axle mount concept to be made in two parts would be the best option to mitigate against angular asymmetry in the rear spaceframe members. This design was further developed, and the final design was as shown in Figure 36. The length of the tube fitting before its shoulder was extended to 60 mm to ensure a significant surface could be painted with methacrylate adhesive and a strong bond could be present with the inside of the tube. This also increased the component's ability to mitigate against longitudinal misalignment.

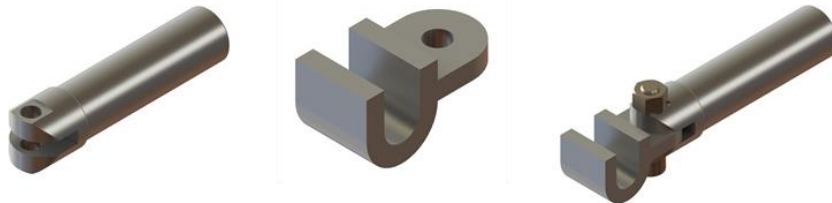


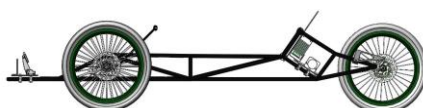
Figure 36 – final design of axle mounting component

Due to a lack of CNC machine time availability, the tube fitting parts were hand manufactured from 25 mm diameter, 85 mm long cylindrical mild steel bars. The challenge of creating the rounded face was overcome using a radial cutter with the part oriented vertically in a milling machine. Though a completely smooth curve profile on the tube fitting face could not be created through this process as seen in Figure 37, the curve was sufficient for the hook piece to experience no impedance of angular adjustment due to sharp corners.



Rounded face that presented manufacturing challenge

Figure 37 – manufactured axle mounting component



STEERING DESIGN

The steering system of this project can be divided into three areas of investigation that would inform the design process:

- Steering geometry and variable angles.
- Interface between steering input and front wheels
- Driver control and actuation method

Steering Geometry and Variable Angles

Introduction to Adjustable Steering Angles

The performance and handling of a steering system depends on several design parameters:

- Kingpin Inclination Angle – refers to the angle between the vertical axis of the wheel when viewed from the front and the pivotal axis of the wheel (Figure 38). The distance between these two axes on the surface of the track is the ‘Scrub Radius’.
- Camber Angle – refers to the angle between the vertical axis of the wheel when viewed from the front and the perpendicular axis to the ground (Figure 39).
- Toe angle – refers to the angle between the direction in which the wheel is pointing when viewed from above and the centreline of the car (Figure 40).
- Caster angle – refers to the angle between the pivotal axis from the wheel when viewed from the side and the perpendicular axis passing through the tyre’s contact patch to the ground (Figure 41). The distance between these two axes on the surface of the track is the ‘Mechanical Trail’.

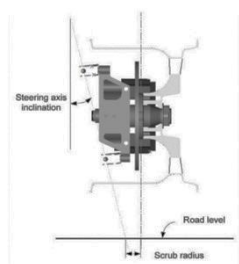


Figure 38- Schematic showing kingpin inclination angle (referred to as ‘steering axis inclination’) and scrub radius (Seward, 2014).

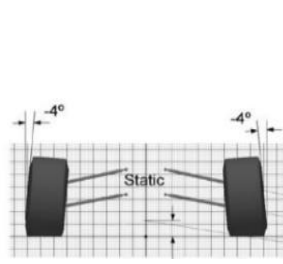


Figure 39- Example schematic showing 4° of negative camber (Seward, 2014).

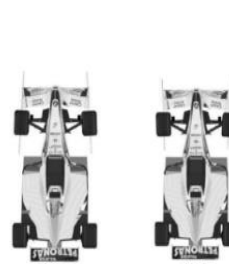


Figure 40- Schematic showing toe angle (Seward, 2014).

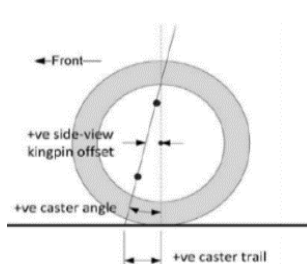
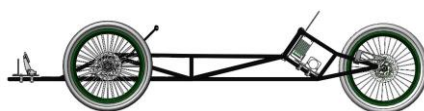


Figure 41- Schematic showing caster angle (Seward, 2014).

Different configurations are preferable depending on the operating conditions of the vehicle.

Therefore, the objective of fuel-efficient operation informed target angles.

Many of the handling characteristics of the vehicle will depend on the type of tyre used. There are a range of different tyre properties such as the rubber compound used or the internal structure of the



tyre that can impact the handling characteristics of the vehicle by affecting contact patches, slip angles, camber thrust, among other tyre-track interface behaviour (Santing et al., 2007). Studying these effects falls outside the scope of this project. However, it was decided that the steering mechanisms should provide sufficient adjustability to allow for optimum toe and camber angles to be selected, through testing, for any chosen set of tyres.

Other design decisions such as caster angle and kingpin inclination are not normally adjustable so they were thoroughly investigated before deciding on the most appropriate choice.

Kingpin Inclination

Looking at the work carried out by Milliken & Milliken (1995), it was discovered that the greater the kingpin inclination angle, the more the vehicle would be raised when the steering wheel is turned because the pivoting axis is not perpendicular to the ground. This increases the effort needed by the driver to turn the vehicle, as they are effectively exerting a force against a component of the weight of the car, but it also helps to centre the wheels during low speed turning. However, increasing the kingpin inclination can add positive camber to the vehicle when turning which is undesirable, making the steering feel unresponsive and causing unnecessary loads to compress the sidewall of the tyre.

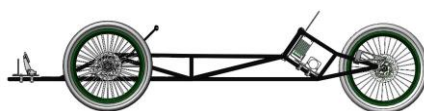
The kingpin inclination also has the effect of providing a design method for altering the scrub radius of the tyre. Reducing this scrub radius reduces the tyre wear by minimising friction between the tyre and the track and it also reduces the moment arm of any braking forces acting on the wheel, resulting in more stable steering under braking.

Minimising the scrub radius (ideally, making it as close to zero as possible) means that the kingpin inclination that can be achieved will largely depend on the clearance available between the wheel hub and the kingpin which is often dependent on other components such as the brake disc, brake caliper or tie-rod mounting.

Caster

The caster angle of the front wheels is the main factor which can aid the self-centering of the wheels after turning. The distance between the contact patch of the tyre and the rotating axis (kingpin axis) of the wheel is referred to as the mechanical trail and it effectively acts as the moment arm for all the lateral forces that are transmitted between the road and the car during cornering.

As the car is effectively undergoing circular motion as it drives around a corner, the lateral forces due to friction are transmitted to the wheel, generating a moment about the kingpin axis. Therefore, increasing the mechanical trail has the effect of increasing the moment generated at the wheels causing the front wheels to have a greater propensity to return to the straight ahead position. This, as



stated by Milliken & Milliken (1995), can be beneficial as it results in more stable and smooth steering at the corner exit but it also results in heavier steering entering the corner as the driver has to effectively counteract the increased moment to turn the front wheels.

Steering Angles Selection

Initial research carried out by the team revealed that the ideal camber and toe angles for a fuel efficiency race should be 0° (Santing et al., 2007). This is in contrast to other set-up configurations used in most racing events where maximum corner speed is usually the determining factor. In this case, the main priority was to reduce all sources of friction and this was found to be achieved by minimising the toe and camber angles.

The kingpin inclination angle should ideally be selected such that a scrub radius of zero is achieved. Based on initial estimations of clearance for other components around the wheel hubs, the maximum kingpin inclination angle would be approximately 17° , measured from the vertical.

Since the kingpin inclination angle has the effect of increasing the camber angle of the wheel while turning, as mentioned in the 'Kingpin Inclination' section, it is important to select a relatively small kingpin inclination angle so that the behaviour of the car is relatively constant and predictable. However, it should not be so small that the advantages of implementing a kingpin inclination angle become insignificant.

The expression for the change in camber angle while turning, due to the kingpin inclination, is given by Seward (2014) as follows:

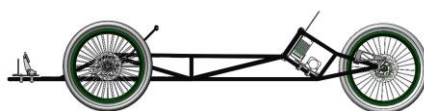
$$\Delta\gamma_k = \theta_k + \cos^{-1}(\sin \theta_k \cos \delta) - 90 \quad (15)$$

In this expression, $\Delta\gamma_k$ is the change in camber due to kingpin inclination, in degrees, θ_k is the chosen kingpin inclination angle, in degrees, and δ is the steering angle (the angle of the front wheel relative to the straight ahead position), in degrees.

Seward (2014) also suggests that the caster angle has an effect on the camber angle of the wheels while turning. However, while the kingpin inclination angle has the effect of adding undesirable positive camber angle, the caster angle has the effect of adding negative camber angle. Therefore, the caster angle of the wheel can be selected so that it counteracts the adverse effects of the kingpin inclination angle while turning.

The expression for the change in camber angle while turning, due to the caster angle, is given by Seward (2014) as follows:

$$\Delta\gamma_c = \cos^{-1}(\sin \theta_c \sin \delta) - 90 \quad (16)$$



In this expression, $\Delta\gamma_c$ is the change in camber due to caster angle, in degrees, θ_c is the chosen caster angle, in degrees, and δ is still the steering angle, in degrees.

Therefore, a total change in camber while turning, $\Delta\gamma_{total}$, in degrees, can be calculated by adding the two expressions above.

$$\Delta\gamma_{total} = \Delta\gamma_k + \Delta\gamma_c \tag{17}$$

This car was designed for an extreme efficiency race. This meant that, ideally, the camber angle should always be zero as this results in the minimum amount of rolling resistance. Therefore, a combination of kingpin inclination angle and caster angle needed to be selected so that the resulting change in camber angle while turning was as close to zero as possible.

Practical design considerations that became apparent further along in the ideation stage of the steering system resulted in the selection of rod-ends to be used as the upper and lower pivot points between the chassis and the wheel hubs. Rod-ends were selected instead of spherical bearings mounted in bearing housings due to their lighter weight, smaller dimensions and ease of mounting without additional fasteners. The line joining these upper and lower pivot points is the kingpin axis. However, these rod-ends, which were to be obtained from RS Components, were commonly found to have a maximum allowable misalignment of $\pm 13^\circ$. Taking this into consideration, the kingpin inclination angle was selected to be 12° which is the highest value that would still allow 1° of misalignment due to expected manufacturing inaccuracies.

A comprehensive analysis was then carried out to observe how different combinations of caster angle and the chosen kingpin inclination angle of 12° would affect the steering system for different steering inputs, the results of which are summarised in Table 22. It was found that a caster angle of 4° resulted in a more stable value of $\Delta\gamma_{total}$ which remained close to zero and negative across all steering angles (positive camber is undesirable as previously mentioned).

Table 22 - caster angle analysis

Steering Input/ °	$\Delta\gamma_{total}/^\circ$ for 2° caster	$\Delta\gamma_{total}/^\circ$ for 3° caster	$\Delta\gamma_{total}/^\circ$ for 4° caster	$\Delta\gamma_{total}/^\circ$ for 5° caster	$\Delta\gamma_{total}/^\circ$ for 6° caster
0	0.00	0.00	0.00	0.00	0.00
5	-0.13	-0.22	-0.30	-0.39	-0.48
10	-0.16	-0.34	-0.51	-0.69	-0.86
15	-0.11	-0.37	-0.63	-0.89	-1.14
20	0.04	-0.30	-0.64	-0.99	-1.33
25	0.28	-0.14	-0.57	-0.99	-1.41
30	0.61	0.11	-0.39	-0.89	-1.39

A summary of the selected steering angles is shown in Table 23.

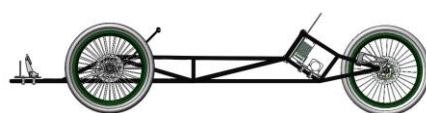


Table 23 - Selected steering angles

Angle	Value/°
Toe	0
Camber	0
Caster	4
Kingpin Inclination	12

It was expected that other factors such as flexing of the chassis under load as well as manufacturing tolerances would result in deviations from the desired toe and camber values. This meant that methods for adjusting these angles were worth implementing in this project.

Steering Linkages Geometry

Different steering geometries were investigated for this project. This refers to the geometric arrangement of the steering linkages which connect the two front wheels together which can have an effect on the behaviour of the car around corners. Ackermann and Reverse Ackermann geometries were investigated.

- Ackermann: When the vehicle is driving around a corner, each of the front wheels travel around an arc of different radius, due to the track width of the vehicle. The Ackermann geometry allows for the inner wheel to rotate more than the outside wheel so that both wheels are pointing in the correct direction, minimising friction between the wheel and the track surface.
- Reverse Ackermann: This is the opposite of Ackermann geometry in the sense that it forces the outside front wheel to rotate by a greater angle than is necessary. This is a set-up often used in high-performance vehicles and is a compromise between improved turning at high speed and added friction between the tire and the track surface. It is clear that this set-up is more beneficial for high-performance competitions which require high corner velocities.

It was decided that the Ackermann geometry would be the best choice for this type of vehicle considering that the main objective was to maximise efficiency. Furthermore, the implementation of Ackermann geometry only depends on the location of the pin joint of the tie-rod connecting the front wheels to each other which means that it does not add any unnecessary complexity or additional components to the design, which is another reason why it was favoured.

Interface Between Steering Input and Front Wheels

Three methods were investigated for transferring the steering input from the driver to the front wheels. These were based on methods commonly used in the automotive industry as well as the previous experience of the Shell Eco-marathon team. An overview and description of each mechanism is provided in Table 24.

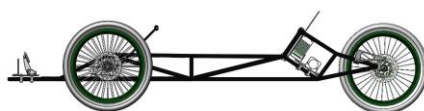
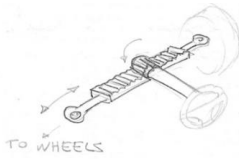
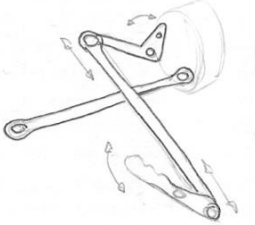


Table 24 - considered steering input to front wheel mechanisms

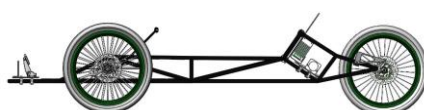
Proposed Idea	Description	Advantages	Disadvantages
<p>1. Rack and Pinion</p> 	<p>Consists of a Pinion attached to the steering column and a rack connected to the front wheels.</p>	<p>Uses components already available from a previous DMT project. Provides greater choice for steering ratio as only the pinion gear would need to be replaced.</p>	<p>Sensitive to misalignment and can be unreliable. Heavier than other options due to the increased number of metal components.</p>
<p>2. Tie-rods on Steering Column</p> 	<p>Consists of connecting the tie-rods from the wheel hubs directly to the steering column (or through the use of a Pitman arm – a lever which extends from the steering column which is rigidly connected to the column).</p>	<p>Implemented in the previous generation Shell Eco-Marathon car and is lighter than other options due to the smaller number of metal components. It is also more reliable as it is a pin-jointed mechanism, which is less sensitive to misalignment.</p>	<p>Wheel angle may not change linearly with steering input angle – depends on the geometry of the Pitman arm.</p>
<p>3. Single lever</p> 	<p>Consists of a lever mechanism mounted at the side of the car and transferring the steering input from the driver to just one of the front wheels directly. A tie-rod is then used to connect the two front wheels together.</p>	<p>Visibility may be improved due to steering system mounted at the side of the chassis.</p>	<p>Slightly more complex than Option 2 due to complex linkage geometry between steering column and front wheel. Little space at either side of the driver so this may interfere with other components.</p>

Using the PDS as a guideline, each idea was evaluated using a decision matrix with the following categories: cost, weight, reliability, ease of mounting to chassis and ease of manufacture.

Weightings were assigned to each category from 1 to 5, with 5 signifying the most important category for this application. Each idea was then ranked from 1 to 3, with 3 being assigned to the idea that best fulfils the requirements of each category. The decision matrix is shown in Table 25.

Table 25 - decision matrix for steering input to front wheel mechanism

Criteria	Weighting	Option 1		Option 2		Option 3	
		Score	Weighted Score	Score	Weighted Score	Score	Weighted Score
Cost	3	1	3	2	6	3	9
Weight	2	1	2	3	6	2	4
Reliability	5	1	5	3	15	2	10
Ease of Mounting to Chassis	1	3	3	2	2	1	1
Ease of Manufacture	4	3	12	2	8	1	4
		Total 1:	25	Total 2:	37	Total 3:	28

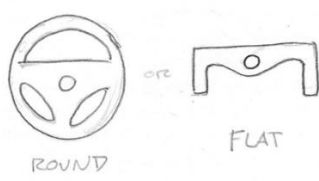
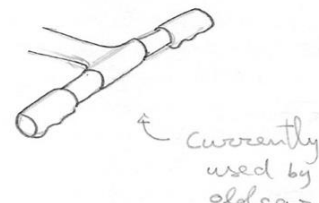
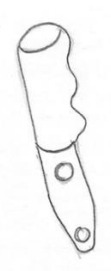


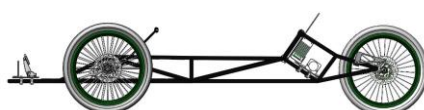
Using the results from the decision matrix shown in Table 25, it was decided that Option 2, consisting of mounting the tie-rods to the steering column, would be the best choice for this application.

Driver Control and Actuation Method

A very similar process was carried out for the driver control and actuation system for the car, which refers to the method through which the driver would interact with the steering system of the vehicle. Four ideas were proposed and they were compared against the requirements described in the Product Design Specification to then select the most appropriate choice through the use of a decision matrix. The options explored are described below.

Table 26 - actuation methods

Proposed Idea	Description	Advantages	Disadvantages
<p>1. Steering Wheel</p> 	<p>Most familiar method for controlling the steered wheels of a vehicle.</p>	<p>More ergonomic than other options and allows the driver to comfortably apply the required steering torque.</p>	<p>Needs to be purchased or careful consideration given to its manufacture due to its complexity. Poor visibility straight ahead due to the low driving position and it may be heavier than other options.</p>
<p>2. Handlebars</p> 	<p>Implemented in the previous vehicle and is similar to the handlebars in a bicycle.</p>	<p>Relatively cheap and simple to manufacture. It is also the best option for easily attaching other components such as a throttle or brake levers.</p>	<p>May provide uncomfortable ergonomics, especially during turning.</p>
<p>3. Lever Handle</p> 	<p>Consists of a single lever stick that would be used to control the wheels. It would be better suited for the 'Single Lever' steering mechanism but it can be adjusted to the requirements of the 'Tie-rods on Steering Column' mechanism chosen.</p>	<p>Lightweight due to the reduced number of parts.</p>	<p>May be difficult to operate and tilt left and right in the confined space of the driver's cockpit.</p>
<p>4. Angled Handlebars</p> 	<p>Similar idea as Option 2 but different configuration of handles.</p>	<p>Ergonomics would be improved by angling the handlebar and offsetting the pivot point vertically so that the driver has more space to operate the steering.</p>	<p>Visibility would be slightly reduced compared to the 'Handlebar' option.</p>



Another decision matrix was implemented at this stage, although the five categories chosen to compare each option were now changed to the following: cost, weight, ergonomics, ease of manufacture and visibility

Weightings were also assigned to each category, from 1 to 5, and each idea given a rank from 1 to 4. The results are shown in Table 27.

Table 27 - decision matrix for actuation methods

Criteria	Weight	Option 1		Option 2		Option 3		Option 4	
		Score	Weighted Score						
Cost	1	1	1	3	3	4	4	2	2
Weight	2	1	2	3	6	4	8	2	4
Ergonomics	5	3	15	1	5	2	10	4	20
Ease of Manufacture	3	1	3	3	9	4	12	2	6
Visibility	4	2	8	4	16	1	4	3	12
		Total 1:	29	Total 2:	39	Total 3:	38	Total 4:	44

Option 4, consisting of the angled handlebars, would be the best choice for this application. One of the main reasons for this is due to the improved ergonomics which is of great importance given the very small space available for the driver inside the car, especially in endurance competitions.

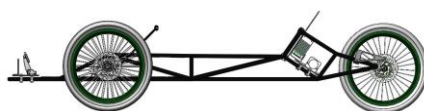
In order to reduce the weight of the car, it was decided to manufacture the steering interface from carbon fibre. However, an angled design would have been difficult to implement without proprietary moulds, increasing the complexity and cost of this option. Similarly, the penalty on visibility was made clear once the complete vehicle was developed using computer aided design.

Ultimately, the decision was made to implement the next best option from the decision matrix analysis. This was Option 2 which consisted of a straight handlebar design. The team were able to reuse the previous prototype Shell Eco-marathon entry’s carbon fibre handlebar steering column with minimal modification required or additional cost.

Steering Design Process

Bearing Selection and Design Considerations

At this stage in the design process, it was already agreed with the supervisor and the team principal that the wheels of the previous generation Shell Eco-Marathon vehicle would be reused for this project. Therefore, the bearings already mounted on their wheel hubs would be reused and the only other bearings that would need to be selected would be those that allow the wheel spindle assembly (consisting of all the components that are mounted directly onto the wheel) to rotate about the



kingpin axis. The bearing selection process shown below corresponds to the analysis carried out for these kingpin axis bearings.

Design Criteria

It was important to determine an estimate for the angular velocity of rotating components in the steering system, even if these would be subject to partial rotations as opposed to complete revolutions. A number of conservative estimates were made based on information previously collected about the track, the regulations and previous experiences.

It was determined that a good estimate for the target turning radius for this vehicle would be 6 metres. Taking into account the selected wheelbase of 1.55 m and a track width of 500 mm, a steering angle, θ , of approximately 15° on the outside wheel was calculated from Equation 18.

$$\theta = \sin^{-1}\left(\frac{\text{wheelbase}}{\text{turning radius of wheel}}\right) \quad (18)$$

This corresponds to a maximum steering angle of 16.3° on the inside wheel as its turning radius is smaller due to the Ackermann steering geometry selected. However, to consider any potential excess steering made by the driver, a conservative maximum steering angle of 20° at the wheels was used for calculations.

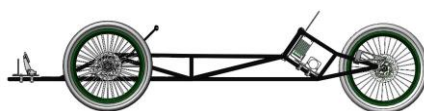
The driver's reaction time was estimated to allow the driver to cover this turning angle in a period of 0.5 seconds. Therefore, the equivalent rotational speed of the wheels rotating about their kingpin axis would be 6.67 revolutions per minute.

This angular velocity would provide a design criterion for the bearings that would support the kingpin axis. However, this value was extremely low as a requirement for rolling element bearings - any rolling element bearing would easily satisfy this requirement. Therefore, other considerations such as load cases as well as efficiency concerns would be more appropriate selection criteria for these bearings.

Load Case

The overall static axial load on the entire vehicle was estimated to be 110 kg, corresponding to 50 kg for the vehicle (including the chassis, steering, powertrain, pedal box and shell) as well as 60 kg for the driver. Note that at the time of calculation, the chassis design was still in its early stages, leading to a conservative worst-case estimate for its mass. A safety factor of 1.2 was applied to this value, as required in the Product Design Specification, resulting in a total static weight of 132 kg to be used as a design consideration.

This value was initially divided up equally across the three wheels to provide an initial estimate of 432 N of axial load acting on each wheel assembly. However, in each of the front wheel assemblies, the



wheel spindles were expected to be connected to the chassis by two bearings, one at the top and another one at the bottom of the kingpin axis. Therefore, the total static axial load on each bearing would be 216 N.

The dynamic axial load on each bearing was also estimated to be 216 N. This value was chosen to be the same as for the static load case because the team learned that the competition would be held at a professional test track consisting of a relatively smooth surface as well as no significant elevation changes and as such a dynamic multiplication factor of 1.2 was considered appropriate.

The dynamic radial load on each bearing was estimated using information provided to this team by the Powertrain DMT team. They estimated that the acceleration produced by the motor would be approximately 0.3 ms^{-2} . Using Newton's 2nd Law of Motion, the force required to produce this acceleration was 39.6 N that would correspond to 13.2 N at each wheel assembly and, therefore, only 6.6 N at each bearing.

Similarly, the maximum tractive deceleration force that could possibly be achieved would correspond to the maximum friction that could be generated between the tyres and the track surface. Using an estimated value of 0.75 for the friction coefficient and a total static vehicle weight of 132 kg, this corresponds to a deceleration force of 971.2 N that would be distributed across all three wheels resulting in 324 N at each wheel and, therefore, 162 N at each bearing. Comparing the maximum acceleration and deceleration forces at each bearing, it was possible to say that the maximum radial load to be expected at each bearing would be 162 N.

The maximum lateral force was also calculated and, similarly to the deceleration force, it would occur when the vehicle is at the point of sliding as it travels around a turn. The analysis results in the same value of 971.2 N of lateral force on the vehicle, corresponding again to 162 N of force at each bearing.

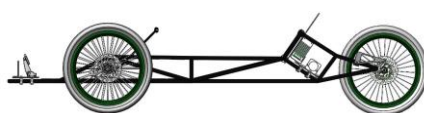
A summary of the maximum value of each type of load acting at each bearing is shown in Table 28.

Table 28 - loading on bearings

Load Type per Bearing	Maximum Value/ N
Static Axial Load	216
Dynamic Axial Load	216
Radial Load	162

Bearing Selection

The bearing type selection chart from 'Mechanical Design Engineering Handbook' (Childs, 2019) shown in Figure 42 was used to select bearings that would satisfy the requirements stated previously.



This low speed and low load application lies within the region for rubbing plain bearings. The operating conditions also lie within the 5 mm diameter region of the graph, in Figure 42. Therefore, as a starting point, bearings with 5 mm internal diameter were investigated.

The final decision was made to use rubbing plain bearings, agreeing with the analysis and selection method using the chart in Figure 42, in the form of spherical bearings mounted on rod-ends. These would allow for misalignment between the top and the bottom kingpin axis mounting points, as mentioned in the ‘Steering Angles Selection’ section of this report. The best option found from available suppliers were the LDK POS 5EC series of rod-ends as these were found to have the desired dimension of 5 mm internal diameter as well as the correct misalignment of 12° required for the kingpin axis inclination implemented in this design.

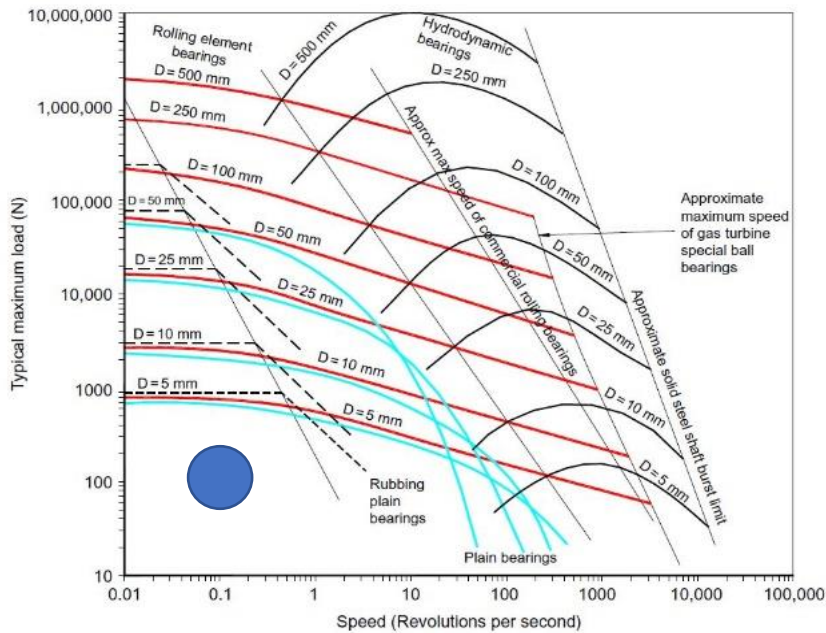
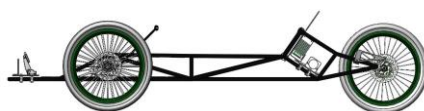


Figure 42 – maximum load against speed chart for spherical bearings

Internal Diameter Bearing Check

It was important to check the required strength for the material that will act as a shaft through both bearings to make sure that a maximum diameter of 5 mm would be sufficient.

Design decisions that were made further along in the embodiment phase of the design stage resulted in the implementation of a threaded rod that would act as the kingpin axis and would, therefore, pass through the top and bottom rod-ends chosen previously. This rod would be mostly loaded in shear due to the lateral forces acting on the car as well as the acceleration and deceleration forces previously mentioned. Therefore, research was carried out into the shear failure mode of bolts, representing the threaded rod selected, and it was found that their shear strength was approximately 60% of the ultimate tensile strength of the material which the bolt is made from (Fastenal, 2009).



The maximum force acting on the bolts in shear would be 162 N. Assuming that the strongest available bolt can be sourced, this corresponds to a Class 12.9 bolt with an ultimate tensile strength of 1220 MPa and therefore a shear strength, τ , of 732 MPa. Using Equation 19, it was determined that the diameter, D , required for the bolt would be 0.5 mm.

$$\tau = \frac{\text{Shear Force}}{\text{Area}} = \frac{\text{Shear Force}}{\frac{1}{4}\pi D^2} \tag{19}$$

If a lower grade bolt is used, which is much more readily available, it would correspond to Class 8.8 properties with an ultimate tensile strength of 800 MPa and a shear strength of 460 MPa. The diameter required for the load case being studied would be 0.66 mm.

In conclusion, even if the lower grade bolts were used, any practical diameter would suffice for this application. This analysis, which highlighted the sufficient strength of 5 mm diameter bolts, made it possible to select M5 or bigger bolts for any mounting requirements throughout the vehicle, with the selection being more dependent on practicality and available components instead of strength.

Provisional Steering Assembly Design

Wheel Spindle and 'L' Bracket Assemblies

Instead of using a decision matrix approach, the iterative nature of this design project meant that it was more beneficial to begin with a basic idea that would then be improved until it satisfied all the design specifications.

The provisional design chosen at this stage of the development process is shown in Figure 43.

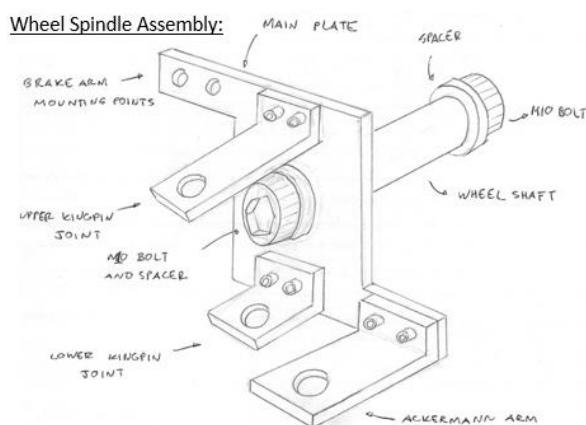


Figure 43a – wheel spindle assembly sketch

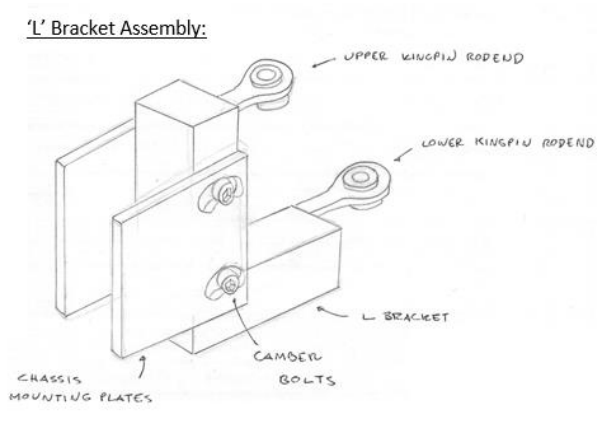
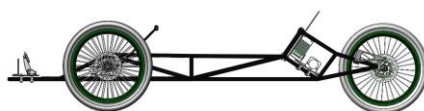


Figure 43b – 'L' bracket assembly sketch

This design consists of two separate subassemblies at each front wheel which are connected by the rod-ends. The subassemblies are as follows.



- Wheel Spindle Assembly: This subassembly will be mounted to the wheels of the car and, therefore, consists of all the components which are required to turn left and right with the wheel. This consists of a main plate that will provide the general structure onto which other components will be attached, two angled brackets which provide the correct kingpin axis inclination, an Ackermann arm that allows the appropriate Ackermann steering geometry to be achieved, a wheel shaft which is stationary and is machined down to the appropriate diameter of the bearings already mounted on the wheels, and appropriate mounting for the brakes which were selected by the Powertrain DMT. All components would be made of aluminium to reduce weight.
- 'L' Bracket Assembly: This subassembly will be mounted semi-rigidly to the chassis and will provide mounting points for the wheel spindle subassembly to connect via the rod-ends. It consists of two chassis mounting plates that will have mounting points to connect to the chassis tubes as well as clearance slots for camber bolts to allow the camber to be adjusted, and an 'L' shaped bracket that will have appropriate mounting points for the rod-ends that will be horizontally offset from each other to provide the correct kingpin axis inclination and caster angles. All components would be made of aluminium to reduce weight.

It was decided that for the wheel spindle assembly, all components should be made separately and then mechanically fastened to the main plate through the use of M5 bolts and nuts. This method presents a weight penalty compared to a unibody design, but it is cheaper to manufacture using in-house methods and also provides greater flexibility for further development of each component. CNC was ultimately implemented to achieve the desired angle for the angled brackets using the facilities available at the Student Teaching Workshop.

Design Considerations

An important design choice was the thickness of all the components to ensure that they could withstand all the forces expected. An example of a critically loaded component was the angled bracket that would effectively act as a built-in cantilever beam. The driver and chassis loads would be transferred by the 'L' bracket rod-ends and be exerted on the angled brackets by spacers mounted on the kingpin axis bolt.

Initially, a thickness of 3 mm was chosen for the cantilever section of the bracket to minimise the total weight. An approximate width of 20 mm was chosen to provide sufficient support for the kingpin

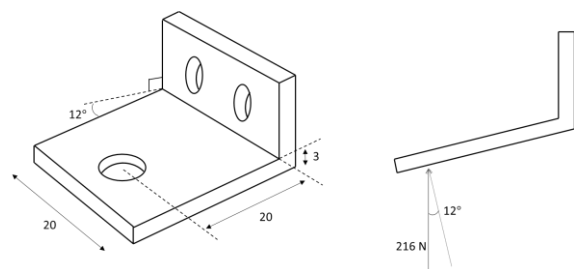
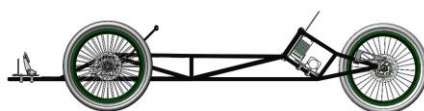


Figure 44 – angled bracket dimensions



axis spacers and a total cantilever length of 20 mm was used as an initial estimate for the length of the angled brackets, as shown in Figure 44.

As mentioned previously, a maximum axial load of 216 N was expected to act vertically at each wheel. This provided a force component of 211 N perpendicular to the surface of the cantilever angled bracket. The bending moment calculations and bending stress analysis were carried out as follows using Equation 6, where the bending stress, $\sigma_{bending}$, is a maximum.

$$M = 211(0.02) = 4.23 \text{ Nm}$$
$$\sigma = \frac{My}{I} = \frac{4.23(0.0015)}{\left(\frac{0.02 \times 0.003^3}{12}\right)} = 141 \text{ MPa}$$

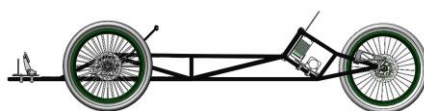
For a 3 mm thick piece of aluminium of the given dimensions, the maximum bending stress was found to be 141 MPa. This was too high for the grade of aluminium available from the ME Stores (6082-T6 grade) which had a yield strength range from approximately 180 MPa to 230 MPa. The same analysis shown above was repeated for a thickness of 4 mm and the maximum bending stress was found to decrease to a value of 79.3 MPa which was acceptable. It was therefore decided that a minimum thickness of 4 mm would be used for all components of the steering system. A 2.5 mm fillet radius was added at the base of all cantilevered components to mitigate the effects of stress concentration.

Brake Caliper Mounting Arm

Another critical feature that needed to be included in the design of the steering system was the mounting for the front brake calipers. Therefore, it was necessary to design the main plate of the wheel spindle assembly to include appropriate spacing for the mounting of an additional bracket, if necessary, to securely hold the brake calipers. The specific selection of the brake caliper parts would be the responsibility of the Powertrain DMT.

The coordinates of the mounting points of the brake calipers on the main plate relative to the axis of the wheel depends on the diameter of brake disc used. The brake disc is the component that is attached to the wheel where the caliper exerts the braking force. Bicycle wheels were to be used in this car which meant that it was necessary to investigate which type and size of bicycle brakes were available from convenient suppliers. This was particularly important considering the modification to the rules and regulations that was introduced for the Shell Eco-Marathon competition in 2020 which required hydraulic brakes to be used throughout the vehicle (Simmons, 2019). It was found that brake rotors were supplied in standard dimensions of 160 mm, 180 mm and 203 mm in diameter.

This was compared to the previous generation car which was found to successfully implement 'TRP 14' 160 mm brake rotors. Therefore, after discussion with the team principal, it was decided that this



vehicle would also use the same dimension for the rotors in an effort to reduce the total weight of the vehicle. This decision was also discussed with the Powertrain DMT who confirmed that these dimensions would provide sufficient braking capacity for the dynamic conditions that this car would experience. Brand new 'Avid HS1' 160 mm brake rotors were found in the Pit Garage, that had significantly less wear than the old parts, were perfectly flat without any warping and could be mounted directly to the same wheels. Therefore, the decision was made to use these new 'Avid HS1' rotors to improve the vehicle's braking capacity at no additional cost.

Mounting Configurations

The type of mounting used for the brake calipers needed to be selected next. Two type of standard mounting configurations (Figure 45) were analysed:

- Post Mount: calipers using this mounting configuration are more readily available. However, mounting holes would be perpendicular to the main plate so an additional bracket would be required.
- International Standard Mount: Less common configuration. However, the calipers could be face mounted directly to the main plate.



Figure 45 – standard brake caliper mounting configurations (Merlin Cycles,2014)

Discussing with the Powertrain DMT and searching for potentially suitable calipers from the available suppliers, it was found that post mount calipers were much more readily available in a range of prices, dimensions and braking capacity. Therefore, the decision was made to design a bracket that would be rigidly attached to the main plate and would provide appropriate mounting locations for post mount calipers for 160 mm rotors.

The Avid technical drawings document (Avid, 2012) proved to be an invaluable source of information for determining the correct mounting points for the required calipers. This information, summarised in Figure 46, provided the correct location of the caliper mounting points relative to the wheel axle.

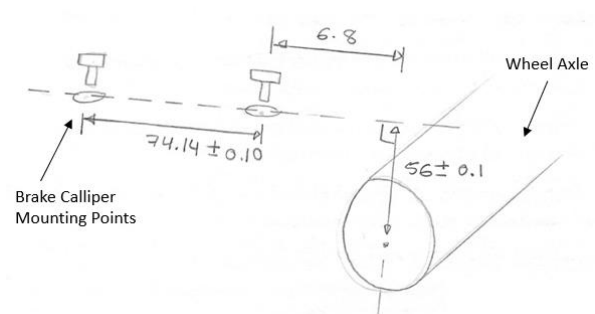
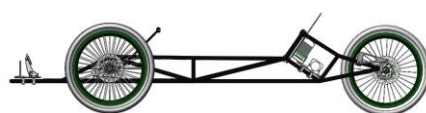


Figure 46 – position of caliper mounting points relative to wheel axle



Using this information, a brake caliper arm was designed that would be fastened to the main plate of the wheel spindle subassembly, shown in Figure 47.

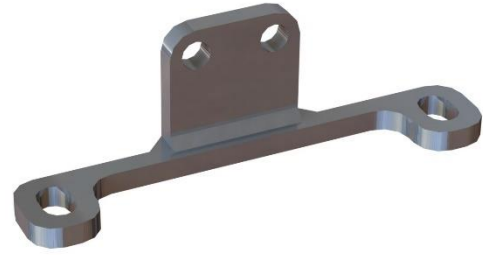


Figure 47 – final brake caliper arm design

Initially, the idea was to mount the brake calipers towards the top of the main plate, as shown in Figure 43a above, where they could be easily accessible if there was a need

to carry out maintenance of the brakes as well as to make sure that they would not interfere with the other steering components. However, careful analysis of the geometric arrangement of the steering components revealed that due to the caster angle of the wheels, the main plate would be at an angle which would raise up the brake calipers, as shown on Figure 48.

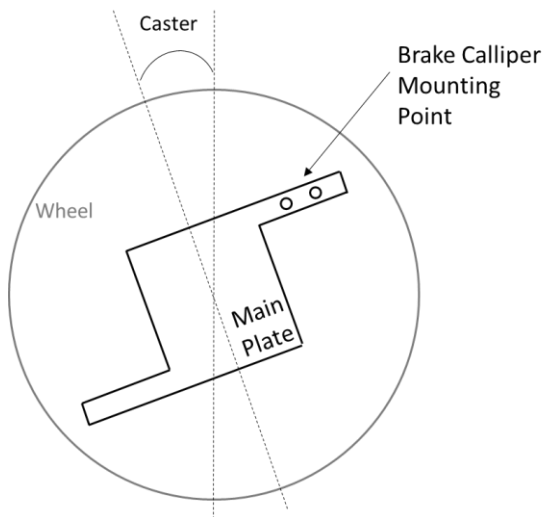


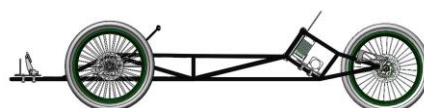
Figure 48 – geometric analysis of steering components

This would have had the effect of increasing the centre of gravity of the car due to the relatively significant weight of the brake calipers and mounting brackets, increasing the risk of rollover. Therefore, a better idea was to mount the brake calipers towards the bottom of the main plate. This is not normally done on road vehicles due to packaging concerns with the suspension components as well as the position being more difficult to access, more exposed to road debris and more prone to pad damage due to flex of the disc under large braking

loads. For this application, the significantly smaller braking loads, the relatively clean track surface and the enclosed design of the vehicle shell which largely protects against debris meant that it would be possible to mount the brake calipers towards the bottom of the main plate.

Steering Column

The steering column consists of all the components that connect the steering interface of the vehicle to the tie-rods that transfer the steering input to the front wheels. The exact mounting of the steering column would depend on the available space towards the front of the chassis. However, the design should ensure that the tie-rod which connects the front wheels to each other should be perpendicular to the longitudinal axis of the vehicle when in its neutral (no steering input) position to ensure that the Ackermann geometry is satisfied.



From the decision matrix previously analysed, it was decided that a handlebar would be used as the steering interface for the driver. This handlebar would have to be rigidly attached to the chassis at least at one location for the driver to comfortably apply the required steering torque. The front of the car was very limited for space but the most suitable mounting point was

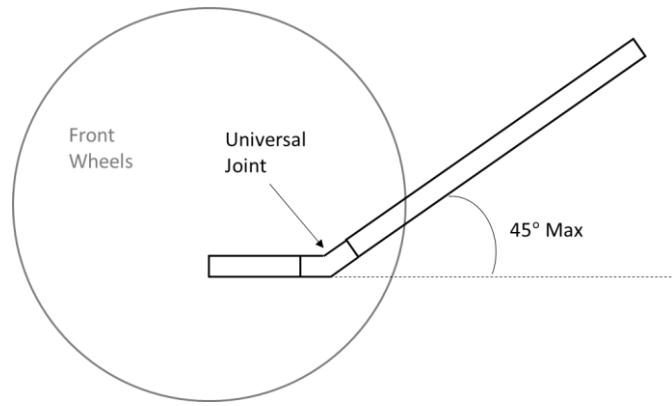


Figure 49 – use of universal joint with handlebar for steering interface

determined to be under the driver’s legs, such that the steering column would go between their legs towards the floor of the vehicle. This was found to be the only option that would not restrict the driver’s visibility but it meant that a mechanism would be required to control the angle between the steering column and the floor of the car where it would be mounted. The best method to solve this was found to be a universal joint that would allow a maximum angle of 45° of elevation for the steering column, as shown in Figure 49, similar to the design used for the previous generation vehicle, which was deemed to be sufficient for the driver to have an ergonomically acceptable driving position.

The connection necessary between the steering column and the tie-rods was chosen to be a single shaft, a Pitman shaft, that would be rigidly connected at one end to the universal joint previously mentioned and at the other end to a lever referred to as a Pitman arm, as shown in Figure 50.

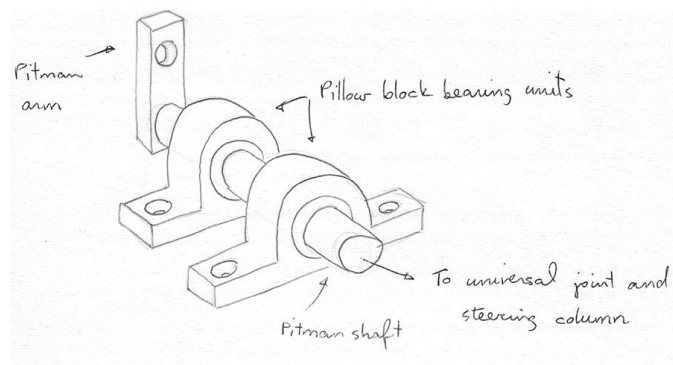
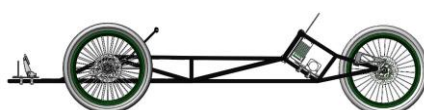


Figure 50 – Pitman connection mechanism between steering column and tie-rods

Ergonomics Consideration

Using a steering angle at the wheel of 15°, appropriate for a 6 m turning radius for a car with a wheelbase of 1.55 m, it was possible to determine the relative motion of the Pitman arm and, hence, the handlebars to decide if the operation of the steering system would be ergonomic. The Ackermann steering geometry caused the tie-rod pivot connection at the wheel spindle assembly to trace a 15°



arc of 37.5 mm radius while turning, corresponding to a horizontal distance travelled by the tie-rod joint of the Pitman arm of approximately 10 mm.

An initial estimate for the length of the Pitman arm which allowed enough clearance for mounting all other components was 30 mm in length, from the axis of rotation to the tie-rod mounting point, as shown in Figure 51.

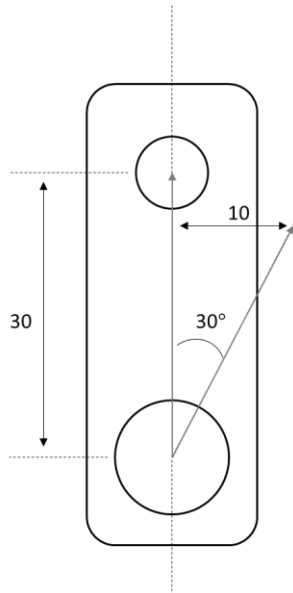


Figure 51 – Pitman arm length

A horizontal distance of 10 mm travelled by the arm would have resulted in an angular rotation of 19.5° of the Pitman arm. Since the Pitman arm was to be rigidly connected to the steering column through the use of a universal joint, this meant that the handlebars at the other end of the steering column would also have to rotate 19.5° . Initially this was found to be acceptable as the driver could comfortably carry out this operation in the limited space of the driver's cockpit. However, increasing the Pitman arm length to 37.5 mm allowed for an improved steering ratio (defined as the ratio between the wheel angle and the steering input angle at the handlebars) of 1:1. This is the same steering ratio that is found in bicycles resulting in a familiar steering sensation for the driver with the added benefit of

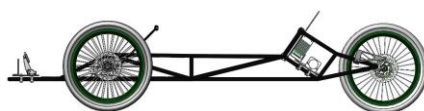
reducing the maximum rotation required at the handlebars from 19.5° to only 15° .

Stress Analysis of Steering Column Assembly

The design of the Pitman arm and Pitman shaft were heavily influenced by the loads experienced by the steering system. It was expected that the loads acting on the Pitman shaft would be due to the lateral cornering forces transferred to the Pitman arm through the tie-rods from the wheels. Axial loads exerted by the driver on the steering system were assumed to be negligible.

Expected Loads

From previous analysis, the maximum lateral force occurring during cornering was calculated to be 323.73 N per wheel. This lateral force would act at the centre of the contact patch between the wheel and road surface which was calculated to be 17.7 mm ahead of the kingpin axis due to the mechanical trail generated by the 4° caster angle and the 254 mm radius of the wheels used (see 'Introduction to Adjustable Steering Angles'). The lateral force would try to self-centre the wheel by creating a moment about the kingpin axis. Therefore, a force transferred through the tie-rod, F , is required to



counteract this moment and to allow the wheel to maintain its course around a corner, as shown in Figure 52.

This tie-rod force would be transferred to the wheel through the pivot point in the Ackermann arm that is located 37.5 mm in front of the kingpin axis.

Therefore, a moment balance made it possible to calculate the tie-rod axial load contribution, F , from each wheel.

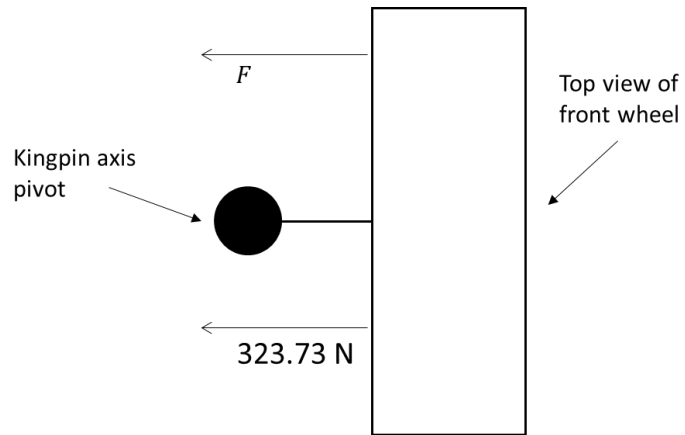


Figure 52 – counteracting effect of lateral force

$$F \times 0.0375 = 323.23 \times 0.0177$$

$$\therefore F = 152.7 \text{ N}$$

Applying a safety factor of 1.2, each wheel would require an axial tie-rod load of 184 N, resulting in a maximum force of 368 N acting at the tie-rod pivot point of the Pitman arm.

A result of this analysis was the decision to mount the Pitman arm on the Pitman shaft as close as possible to the nearest supporting bearing to minimise bending moments through the Pitman shaft. However, a more significant consideration was the torsional deflection of the shaft.

Torsional Deflection of Pitman Shaft

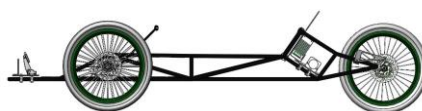
The torsional deflection of a shaft is characterised by the Equation 20, where θ represents the angular deflection in radians, T is the applied torque, L is the length of the shaft, G is the shear modulus of the material of the shaft and J is the second polar moment of area for a shaft of diameter, D .

$$\theta = \frac{TL}{GJ} \tag{20}$$

$$\text{where } J = \frac{\pi D^4}{32} \tag{21}$$

The length of the Pitman shaft was expected to have an upper bound of 100 mm in order to minimise space and total weight. Similarly, aluminium (6082-T6 grade with a shear modulus, G , of 26 GPa) was initially considered due to its lightweight properties compared to steel. The total moment exerted on the Pitman shaft was calculated from the length of the Pitman arm as well as the tie-rod axial forces calculated previously.

$$T = 368 \times 0.0375 = 13.8 \text{ Nm}$$



Using these values and Equations 20 and 21, it was possible to calculate the minimum required second polar moment of area and, therefore, the minimum required Pitman shaft diameter that would result in a maximum acceptable torsional deflection taken to be 0.5°.

$$J = \frac{TL}{G\theta} = \frac{13.8 \times 0.1}{26 \times 10^9 \times 8.7 \times 10^{-3}} = 6.08 \times 10^{-9} \text{ m}^4$$

$$\therefore \frac{\pi D^4}{32} = 6.08 \times 10^{-9}$$

$$\therefore D = 0.016 \text{ m} \Rightarrow 16 \text{ mm}$$

This result suggests that the minimum diameter of the Pitman shaft was required to be 16 mm if it was to be made from the aluminium material available. The same calculation was repeated for mild steel, with a shear modulus, G , of 79.6 GPa, resulting in a minimum required diameter of 12 mm.

Although the required steel shaft would be heavier than the required aluminium shaft, the smaller diameter meant that smaller bearings, bearing housings, universal joints and bolts could be used that would decrease the overall weight and space required of the steel shaft option compared to the aluminium shaft alternative. Therefore, the mild steel Pitman shaft option was selected.

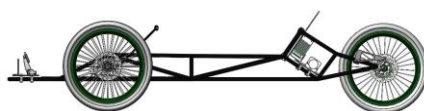
Mounting of Pitman Arm on Pitman Shaft

The Pitman arm could be secured in place on the Pitman shaft through the use of a set screw, a key and corresponding keyway or from the friction provided by a nut screwed into the Pitman shaft. The latter option would be the most convenient as it would not require any additional features to be designed into the Pitman arm or shaft apart from an external thread on one end of the Pitman shaft. The only important consideration was to ensure that the nut could be tightened hard enough so that the 13.8 Nm torque generated by the Pitman arm would not cause it to come loose.

Table 29 shows the average recommended tightening torques for readily available Grade 8.8 steel nuts compiled from different fastener suppliers, including Grampian Fasteners (2017), Fastener Mart (2015) and William Tools Co. (2019).

Table 29 - tightening torques for Grade 8.8 steel nuts

Standard Nut Size	Average Recommended Tightening Torque/ Nm
M5	7
M6	11.8
M8	28.8
M10	57.3
M12	99.8



It was found that M8 nuts or larger could be tightened during assembly to a torque greater than that exerted on the nut by the Pitman arm. Ultimately, since this was a critical component for the safe operation of the vehicle, an M10 nut was used to secure the Pitman arm onto the Pitman shaft.

Stress Calculations of Pitman Arm

Another design consideration was the geometry of the Pitman arm to ensure that it would not yield under the maximum tie-rod loads described previously. As shown in Figure 50 above, the Pitman arm is a lever that can be considered as a cantilever beam built-in at the point where it is connected to the Pitman shaft. The maximum bending moment experienced by this component would be 13.8 Nm as derived previously. An initial estimate for the thickness of this component was 4 mm as this was successfully implemented in other components in the steering system. Similarly, an initial breadth of 11 mm was used to minimise the total weight of the components. Using Equation 6 as before, the maximum bending stress for this geometry was found to be 171 MPa, as shown below, which was too high compared to the yield strength of aluminium.

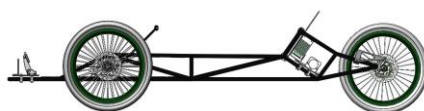
$$\sigma = \frac{My}{I} = \frac{13.8(0.0055)}{\left(\frac{0.004 \times 0.011^3}{12}\right)} = 171 \text{ MPa}$$

The calculation was repeated using a breadth of 16 mm resulting in a maximum bending stress of 80.9 MPa. This was acceptable and made it possible to manufacture this component from aluminium instead of steel without increasing the size significantly, reducing the weight of this component.

Pitman Shaft Bearing Selection

A decision required for the design of the steering column components was to select appropriate bearings for the Pitman shaft. As mentioned previously, the axial loads were taken to be negligible and the maximum radial load would be 368 N. At least two bearings would be required to support the shaft which is why pillow block bearings, also referred to as pedestal bearings, were preferred as they would not need separate bearing housings to be designed and manufactured and they could be installed directly on the floor of the vehicle. The majority of metal pedestal bearings available from approved suppliers were found to be very heavy (approximately 500 grams each) and expensive (approximately £20 each). Therefore, polymer bearings were investigated, paying careful attention to their load ratings.

A much more lightweight and affordable solution was found in the 'IGUS KSTM-12 mm' pedestal bearings, made from impact resistant and rigid thermoplastic composite material. The maximum static radial load rating was found to be 2200 N for short term operation and 1100 N for long operation, both adequate for the required use. Therefore, two of these pedestal bearings were



chosen to be mounted directly on the floor panels of the chassis to support the Pitman shaft and the steering column components.

Tie-rod Selection

Lastly, an appropriate material needed to be selected for the tie-rods, which would be loaded in tension and compression only due to their pin-jointed structure, to ensure that they would not fail by buckling. Therefore, it was important to compare the axial loads acting on the tie-rods to the minimum force required for buckling, P_c , shown in Euler's buckling formula for a pin jointed truss.

$$P_c = \frac{\pi^2 EI}{L^2} \quad (22)$$

To reduce weight, the team decided to try to implement the smallest available diameter of roll wrapped carbon fibre tubes due to their high strength to mass ratio. The smallest available tubes from Easy Composites Ltd, an approved supplier for this project, had an outer diameter of 10 mm and an inner diameter of 8 mm. The flexural rigidity for these tubes, corresponding to EI , was obtained directly from the supplier (Easy Composites Ltd, 2019) and found to be 30 Nm². After making an initial model of the steering assembly, the distance from the Pitman arm tie-rod joint on the steering column assembly to the Ackerman arm tie-rod joint on each wheel was 172.4 mm. This information was then used to determine the critical load for buckling from Equation 22.

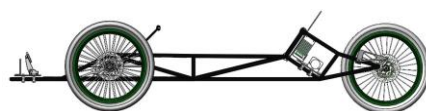
$$P_c = \frac{\pi^2 \times 30}{0.1724^2} = 9961 \text{ N}$$

This critical load for buckling is significantly higher than the expected 184 N of maximum axial load that will be experienced by the tie-rods. Therefore, it was determined that buckling would not be a potential failure mode for this component. However, it was also necessary to investigate potential failure by tensile or compressive yield.

The axial ultimate tensile stress of the 10 mm outer diameter and 8 mm internal diameter carbon fibre tubes was also obtained from the supplier (Easy Composites Ltd, 2019) and found to be 600 MPa in tension or 570 MPa in compression. The geometry of these chosen tubes resulted in a cross-sectional area of 2.83x10⁻⁵ m². The maximum axial stress on the tie-rods was then calculated as follows.

$$\sigma_{axial} = \frac{Force}{Area} = \frac{184}{2.83 \times 10^{-5}} = 6.51 \text{ MPa} \quad (23)$$

The maximum axial stress was found to be significantly lower than the reported tensile or compressive ultimate tensile stress confirming that these would also not be potential modes of failure. Therefore, the selected carbon fibre tubes were deemed acceptable for this application.



Mounting of Steering System to Chassis

The steering column assembly would be connected to the floor of the chassis, approximately below the driver's knees using M5 bolts, nuts and washers on the two pillow block bearings that would constrain the Pitman shaft assembly and steering column. This would only allow the column to be tilted upwards up to an angle of 45° due to the universal joint, to allow the driver to comfortably get into and out of the car and to be able to steer the vehicle in a more ergonomic position.

The wheel spindle assemblies were a more difficult challenge because they involved connecting the 'L' brackets mentioned previously to the round chassis tubes in a way that also provided sufficient angular adjustment to change the camber setting of the vehicle.

An option was studied and developed which consisted of using a pair of two-piece shaft collars that could be tightened around the appropriate tubes and would provide mounting points for plates that would have slots cut out in order to provide the required angular movement for the camber adjustment of the 'L' bracket and wheel spindle. The chosen configuration is shown in Figure 53.

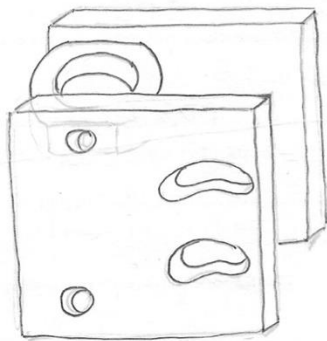
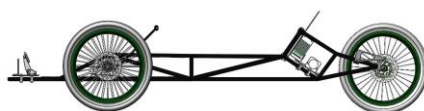


Figure 53 – steering to chassis mounting mechanism concept

The chosen collars were 'RULAND OF-MSP-20-A' which were made of aluminium in order to keep the total weight to a minimum, compared to the other option which used mild steel. These collars were very suitable for this application because they had flat sides and M6 tapped holes already machined into each side, providing an ideal mounting surface for the chassis plates with the camber slots. This option was much more expensive than the adhesive alternative or other simpler shaft collars available.

However, other more affordable options would have required the team to machine flats and tapped holes on the circular surfaces of the collars which would have required significantly more manufacturing time. The added cost of this option was justified.

The only remaining task involved the design of the plates which would include the slots for the camber adjustment of the wheels. The most important design consideration was to ensure that the slots were long enough to allow for a $\pm 3^\circ$ adjustment of the camber setting, as required by the product design specification. The remaining dimensions of these plates and positioning of the slots were selected to ensure that the adjustment in camber setting would result in no change to the track width which is measured from the centre of the contact patches of the front tyres, according to the official 2020 rules (Simons, 2019). The thickness of the plates was also set to 4 mm as this resulted in a maximum bending stress of 28 MPa on each plate due to the maximum braking forces which was acceptable for the grade of aluminium being used (6082-T6 grade).



Final Steering Assembly Design

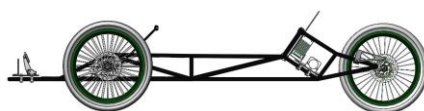
Very slight modifications were made to the provisional design to satisfy manufacturing considerations and to increase the ergonomics of the driver inside the car:

- The main plate was modified slightly to include diagonal supports between the longer parts that extended past the central section of the plate, which is where the brake and Ackerman arms were connected, for added rigidity.
- The location of the mounting points for the brake and Ackerman arms were modified so that the Ackerman arm and tie-rods would now be facing the front of the vehicle. This allowed the steering column to be mounted a few centimetres forward to increase the space in the driver's cockpit.
- The tie-rod configuration in the steering system was modified to include a single drag-link that extends from the Pitman arm to the front right wheel, with a tie-rod then connecting the right wheel to the left wheel directly. This configuration allowed the Ackerman steering geometry to be preserved for all steering inputs.

The final steering assembly is shown in Figure 54.



Figure 54 – final steering system design



Manufacturing and Assembly of Steering System

The majority of the components required for the steering assembly were to be manufactured from 6082-T6 aluminium that could be sourced directly from the ME stores. The fasteners required for the assembly of this system were also sourced from the ME Stores and were made from mild steel. Other components that would be purchased from external suppliers were the rod-ends for the 'L' bracket subassemblies as well as the carbon fibre tubes used for the drag-link and tie-rod components. These were purchased from RS Components and Easy Composites Ltd, respectively.

Manufacturing Methods of Components

A discussion with Paul Woodward and Neil Beadle, responsible for fulfilling laser cutting and CNC requests, respectively, revealed that the number of parts that each DMT team could request to be manufactured by these methods would be very limited. Therefore, these were kept to a minimum.

The final list of steering parts that were requested to be laser cut were as follows:

Table 30 - steering parts for laser cutting

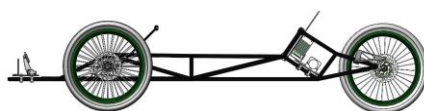
Part Name	Part Description	Quantity
ST-MAIN-PLATE-01-P	Main plate of wheel spindle subassembly.	2
ST-PITMAN-ARM-01-P	Pitman arm where drag-link connects to steering column.	1
ST-CHASSIS-PLATES-01-P	Plates which connect the steering system to chassis, providing camber adjustment.	4

Similarly, the final list of steering components that were requested to be manufactured on the CNC milling machine were as follows:

Table 31 - steering parts for CNC milling

Part Name	Part Description	Quantity
ST-ANGLED-BRACKET-BOTTOM-01-P	Bottom angled bracket of wheel spindle subassembly.	2
ST-ANGLED-BRACKET-TOP-01-P	Top angled bracket of wheel spindle subassembly.	2
ST-BRAKE-ARM-01-P	Brake caliper mounting arm.	2

The angled brackets were required to have an angle of 102° between the inner faces to satisfy the kingpin axis inclination requirement described in the design of these parts. This would be difficult to produce accurately by manual machining which is why they were included in the CNC list. Similarly, the brake caliper mounting arms required a complex shape to allow for the mounting of a wide range of standard bicycle brake calipers which is why they were also submitted as a CNC milling request.



The laser cutting process was a much quicker process which is why the team decided to use it as a method for manufacturing all planar parts of the steering system including the chassis mounting plates which featured camber slots for which the tolerance of the laser cutting process (± 0.2 mm) was deemed acceptable.

The remaining components of the steering system, shown in Table 30, were manufactured manually.

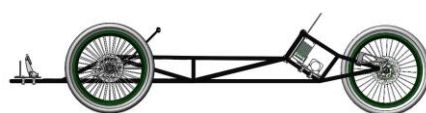
Table 32 - manually manufactured steering components

Part Name	Part Description	Quantity
ST-ACKERMANN-ARM-01-P	Mounting point on wheel spindles for tie-rod.	2
ST-KINGPIN-SPACER-LONG-01-P	Long kingpin axis spacer.	2
ST-KINGPIN-SPACER-SHORT-01-P	Short kingpin axis spacer.	4
ST-L-BRACKET-LEFT-01-P	Left 'L' bracket.	1
ST-L-BRACKET-RIGHT-01-P	Right 'L' bracket.	1
ST-M5-STUDDING-130-01-P	130 mm M5 threaded rod, acting as kingpin axis.	2
ST-PITMAN-SHAFT-01-P	Pitman shaft of steering column.	1
ST-RODEND-SPACER-3-01-P	3 mm rod-end spacers.	11
ST-SHAFT-01-P	Main front wheel shafts.	2
ST-SHAFT-SPACER-01-P	Shaft spacers used at either end of each wheel shaft.	4
ST-TIEROD-INSERT-LEFT-01-P	Tie-rod insert with internal left-hand M5 thread.	2
ST-TIEROD-INSERT-RIGHT-01-P	Tie-rod insert with internal standard M5 thread.	2
ST-DRAGLINK-SHAFT-01-P	Carbon fibre drag-link tube.	1
ST-TIEROD-SHAFT-01-P	Carbon fibre tie-rod tube.	1

Manufacturing Progress

A manufacturing plan was implemented to ensure that responsibilities were distributed evenly among all team members, taking advantage of the individual strengths of each person regarding their previous workshop experience. This manufacturing schedule, which can be found in the Project Quality Plan document of this project (Al-Shabazz, et al., 2020), made it possible to complete the manufacturing of the steering system well within the available time.

The components shown in Table 30 required mostly manual turning, while others required manual milling. Similarly, several of the parts that were submitted to be manufactured by CNC milling were returned with a number of operations still remaining, such as the manual filleting of sharp corners and the drilling of the required mounting holes using the milling machine shown in Figure 55.



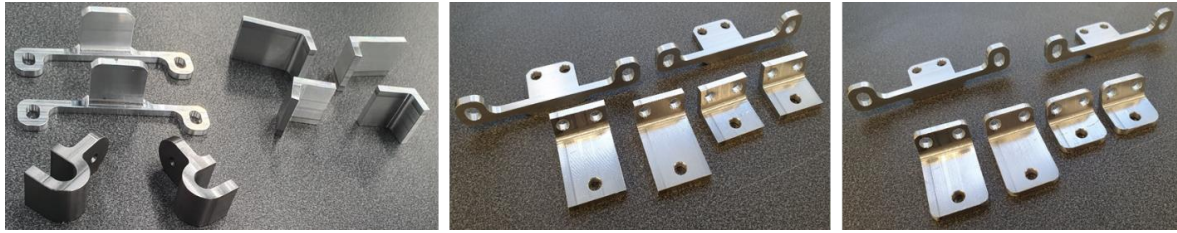


Figure 55 – manufactured steering components

Remaining components such as the kingpin axis spacers, the wheel shaft spacers, the Ackermann arms and the Pitman shaft were also manufactured manually due to their simple shape which allowed the wheel spindle subassemblies to be completed, as shown in Figure 56.

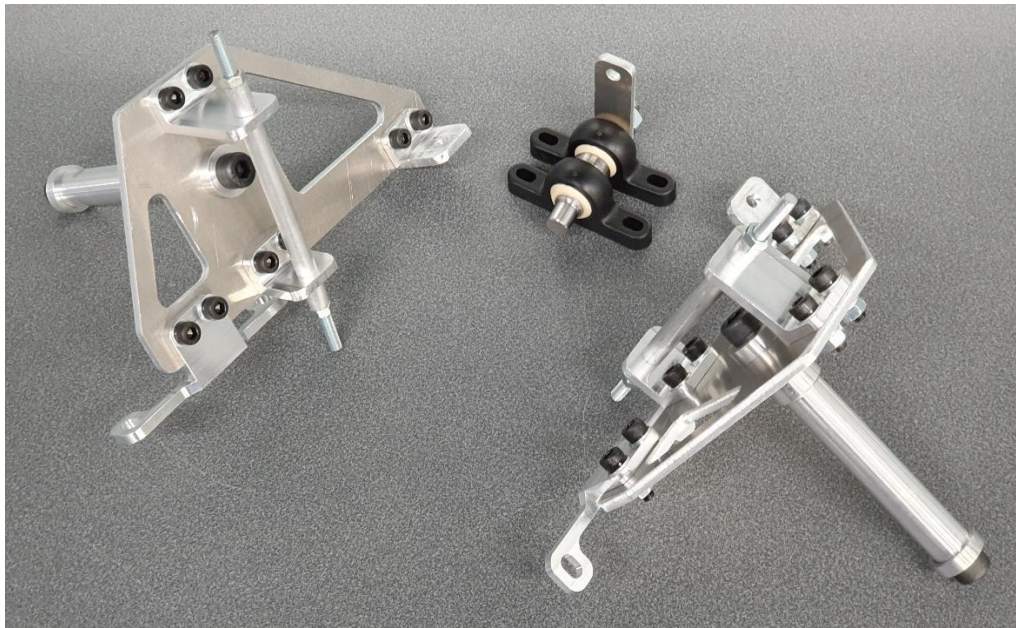
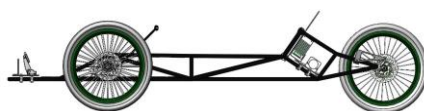


Figure 56 – wheel spindle subassemblies

Some components of the steering assembly, such as the Pitman shaft and the 'L' brackets, required a small amount of time more than was initially anticipated. However, other components, such as the drag-link and tie-rod carbon fibre tubes and their inserts were manufactured without significant setbacks. Overall, the distribution of manufacturing jobs across all members of the team allowed the steering assembly to be completed in the time expected.

Mounting of Steering Assembly onto the Chassis

After the bonding of the chassis carbon fibre tubes was completed, the shaft collars that were used to mount components onto the chassis were fitted around the tubes at their required locations. To mount the steering system to the chassis it was necessary to securely attach two of these collars to each side of the car at the front vertical tubes of the chassis.



The collars were chosen to have an internal diameter of 20 mm to match the external diameter of the tubes. However, the location of these collars was required to be very close to the joints where additional layers of carbon fibre were added in the wet lay-up process to join several tubes together. Figure 57 shows the increased diameter of the tubes where these collars needed to be mounted.



Figure 57 – effect of lay-up on member diameter

Significant manual filing was required, following the required health and safety consideration to minimise exposure to carbon fibre dust, to reduce the effective diameter of the tubes at those locations and to allow the collars to clamp around the tubes as intended. Particular attention was given to the amount of filing necessary to minimise the number of fibres that would be compromised by the cutting action of the filing process.

The mounting process of the steering system onto the chassis was then continued, leaving only the steering column subassembly to be incorporated. The two front wheel spindle assemblies were then connected together using the tie-rod. Following this, the drag-link was connected to the front right wheel spindle assembly at one end, with the other end being connected to the Pitman arm that had been already fastened to the Pitman shaft. The last step of the process involved fastening the two pedestal bearings which support and constrain the Pitman shaft onto the floor of the vehicle.

It was observed that the tie-rod would collide with the drag-link and the Pitman arm at the most extreme steering input angles. To solve this, a riser was prototyped to elevate the Pitman shaft and pedestal bearing assembly to prevent interference with the tie-rod. This marked the completion of the design, manufacture and assembly phases of the steering system which is shown in Figure 58 mounted to the chassis with the front wheels removed.

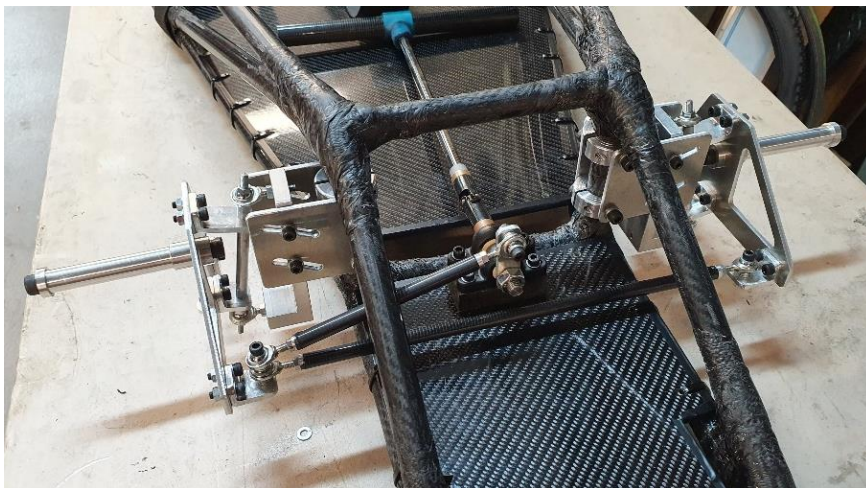
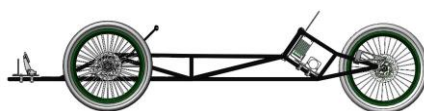


Figure 58 – complete assembly of steering system



TESTING AND MODIFICATIONS

One of the most important parts of this project is the testing of all the components that have been designed and manufactured. The main purpose of this process is to corroborate the proposed designs to determine whether they contribute to the main aims and goals of the project in the way that was intended. Additionally, the testing phase provides a final opportunity to observe which components could be modified to enhance the functionality of the overall product, an example of which was the steering column riser that had to be implemented.

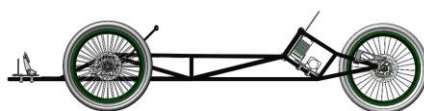
An extensive testing phase for the entire vehicle had been formulated in the Product Quality Plan for this project (Al-Shabazz et al., 2020a). However, this plan was abruptly halted due to the lockdown, forcing the team to suspend all further testing. Nonetheless, a significant amount of very valuable information was collected through limited testing in the remaining days of the project.

Components Inspection

One of the methods in which the vehicle was tested involved setting the vehicle on the ground and allowing a 60 kg person to climb onto the car, holding all three wheels to prevent the vehicle from moving. With the test subject sitting on the car, steering linkages and components were inspected.

The chassis was initially set up with zero toe angle as well as with zero camber angle. However, under the load exerted by the driver's weight, the camber angle was found to change to 2° of negative camber. This was a very significant change that would have observable effects on the handling characteristics as well as reducing the overall efficiency of the vehicle. This, however, was not an unexpected observation. It was known from the beginning of the project that the required lightweight nature of all the components of the vehicle, including the chassis, would inevitably result in a less stiff structure overall that would potentially deflect under load. This was the primary reason to include a method for adjusting the camber angle even though it was agreed that zero camber would be beneficial under all conditions.

To correct for this change in camber angle under load, the team proceeded to pre-set the camber to 2° of positive camber, when unloaded, so that the loads exerted by the driver would then correct the angle to the required 0°. However, it is important to note that this adjustment is dependent on the exact weight of the driver as well as the weight distribution of the vehicle after all components have been mounted, including the powertrain parts and the shell. Therefore, the set-up configuration would have to be repeated once all of these factors have been finalised.



Another area of improvement that was discovered during the testing procedure of the steering components was the chosen universal joint for the steering column assembly. This part was found to break easily once the driver applied minimal effort on the handlebars to try to turn the front wheels, as shown in Figure 59.



Figure 59 – failure mode of universal joint

This failure was also not unexpected due to the plastic construction of the universal joint. However, if this part would fail, it was expected to do so under

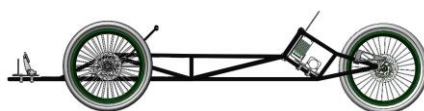
the dynamic conditions of the competition, were the torque exerted on the universal joint could reach values up to 13.8 Nm which would be higher than the rated strength of the plastic casing. The team then proceeded to select a replacement steel universal joint from RS Components that would satisfy the strength requirement as well as the diameter requirements determined by the other parts that had already been manufactured, such as the Pitman shaft.

This universal joint, however, could not be purchased and implemented due to the abrupt ending of the final stages of the project due to the COVID-19 situation. It is for this reason that the team refurbished the broken component and mounted it on the steering column system to serve as an indication of what the final assembly would have looked like.

Ergonomics Testing

An important design consideration that became a priority during the design phase of this vehicle was the driver ergonomics. This is particularly important in this type of endurance competition where the driver will be in an enclosed cockpit for an extended period of time. Therefore, every effort was made to ensure that the driver would be as comfortable as possible, not only sitting inside the car but also while operating the steering interface that was selected for this vehicle.

A valuable piece of feedback received from the test driver sitting in the car was that the steering column was too short, making it uncomfortable to lie back on the seat of the car while at the same time trying to reach for the handlebars, as shown in Figure 60 below. The team decided that the steering column needed to be increased in length from the original value of 350 mm. However, the length could not be extended too much because that would bring the handlebars too close to the driver's chest causing their elbows to uncomfortably extend outwards, potentially colliding with the vehicle's chassis or shell while turning. Therefore, the decision was made to extend the column by



200 mm. It had been planned to implement this by purchasing a replacement carbon fibre tube of the correct dimensions, although this could not be completed due to the COVID-19 situation.



Figure 60 – ergonomic testing

Regulation Compliance

One of the technical requirements for the Shell Eco-marathon Prototype Class of vehicles is that they must have a turning radius of 8 metres or less (Simmons, 2019). This requirement would be tested at the competition by making the car follow a 90° arc of a circle and ensuring that the radius described by the car's motion is 8 metres or less. The process would be repeated for both turning directions.

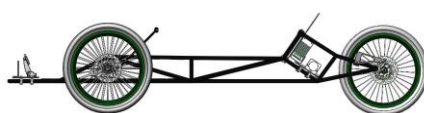
To ensure this vehicle satisfied this specification, the car was taken to the service road directly outside the Pit Garage, where a semicircle of 8 metre radius was marked on the ground using masking tape.

The test procedure used to ensure that the car would pass the same test at the competition began by aligning the outside tyre with the semicircle markings so that the wheel was tangential to this semicircle, with the steering being set to full-right lock, as shown in Figure 61.



Figure 61 – turning radius test

The car was then manually pushed forward, while holding the full-right lock on the steering system, until the external wheel was at 90° relative to its starting position, as demonstrated by Figure 62. This would mean that the car had travelled along a 90° arc as required by the rules which would then allow the turning radius to be measured.



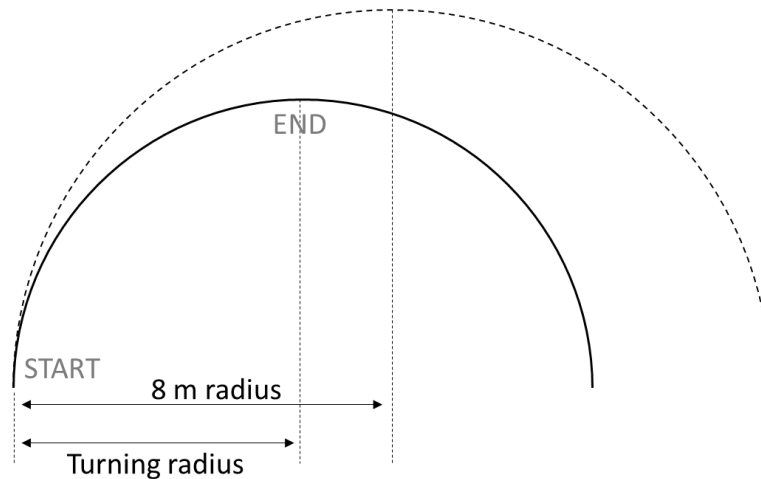


Figure 62 – turning radius test results schematic

The tests were carried out twice in each direction to ensure reliability of the results and it was found that the turning radius to the right was 6.35 m while the turning radius to the left was 5.15 m. The difference in turning radius for each direction was believed to originate from small differences in wheel alignment, due to the individual camber adjustment of each wheel. A small misalignment could, therefore, result in very noticeable differences in turning radius, as was the case in this test. Nonetheless, both turning radii recorded passed the required turning radius test comfortably.

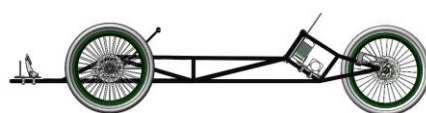
This test was carried out without a driver sitting in the car in order to mitigate all potential risks associated with the test and to be able to obtain a value that could be used for reference. However, a more accurate result would have been obtained with all other systems mounted on the car, including the powertrain components and the shell, with the designated driver sitting in the car and with the wheels correctly adjusted to minimise the turning radii difference due to turning direction.

Additional Planned Testing

A number of additional tests had been planned, not only to ensure that the steering system would be rule compliant, but also to maximise the efficiency of the vehicle during race. However, these tests could not be carried out due to the COVID-19 disease outbreak.

The regulations require the steering system to be designed in such a way that the wheels would never come into contact with any other components of the car such as the chassis, the shell or the wheel bulkheads mandated by the rules (Simmons, 2019). This was due to be investigated after the shell had been mounted onto the chassis and with a driver sitting inside the car who could provide visual feedback of the results.

The effectiveness of the M5 threaded rod acting as the kingpin axis of the steering system was also going to be investigated to ensure that it could withstand the dynamic loads exerted on the front

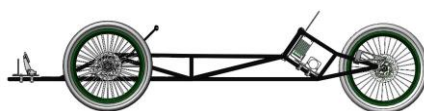


wheels during competition conditions. This test could only be performed once the motor and battery were installed on the vehicle and the procedure would consist of inspecting those components before and after a test run, looking for noticeable permanent deflection or failure of the threaded rod. A simpler test was also planned to be performed by applying a relatively high number of cycles of static loads, simulating the driver getting into and out of the car. The limited amount of testing that was carried out showed no indications that this component could cause any problems, even after having several test drivers of above 60 kg sit in the car.

A more qualitative test was also planned to evaluate the entire steering assembly as a whole. One of the most important characteristics of a steering system is the feedback it provides to the driver about road conditions as well as the transfer of loads and the vehicle dynamics of the car. This is more difficult to measure and depends on a number of factors ranging from the angles chosen in the initial set-up of the vehicle to the rigidity of the components used. An important test that had been planned was for a test driver to follow a simple test track layout that would allow them to get a feel for the accuracy of the steering system as well as to relay other important feedback including any observed deflections, vibrations or the general responsiveness of the car. This test would also evaluate the ability of the car to self-centre the wheels on the exit of a corner and the steering effort that would need to be applied at the handlebars to be able to turn the car.

The effectiveness of the braking system also needed to be investigated to ensure that the driver could apply sufficient braking force to keep the car stationary at a 20 % incline, as mandated by the regulations (Simmons, 2019). This would have been carried out towards the end of the testing phase as it required the entire vehicle to be fully assembled, including the shell, the powertrain components and the driver sitting in the vehicle to account for all the components that would have added mass to the finished vehicle. The results of this test would have allowed a judgement to be made regarding the efficacy of the brake disc diameters and brake calipers selected by the Powertrain DMT group.

A critical component requiring further testing was the aluminium plate that would separate the driver's cockpit and the powertrain compartment and which would act as the roll panel that would protect the driver in the event of a rollover accident. This panel was designed to withstand a minimum of 700 N of force applied in any direction along its top edge, as required by the regulations (Simmons, 2019). Nonetheless, further testing had been planned using a fixture that would allow loads greater than 700 N to be exerted on the plate to mitigate against any possible material defects that could become a safety concern for the driver.

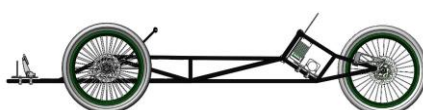


BUDGET

The total budget for this project was £5000, of which £1000 was from the department of mechanical engineering and the remaining budgeted by the Shell Eco-Marathon team principle. In total £1325 was spent, the biggest cost was the lightweight carbon fibre chassis and safety equipment, as well as the shaft collars necessary for secure mounting of components to the spaceframe. The amount spent was in line with similar past projects, a full overview of spending's is given below.

Table 33 - spending overview

Area	Supplier	Description	Cost (£)
Spaceframe	Easy Composites Ltd	15x1m Carbon fibre tubes, Carbon Fibre narrow fabric plain weave 25mmx15m, 50mmx15m, Composite shrink tape, 50ml methacrylate adhesive 1kg EL2 epoxy laminating resin + AT30 hardener	430.09
	Advanced Hackspace	ABS+ 3D printed Lugs (x20)	20.00
Steering	ME Stores	4mm thick aluminium sheets D8,10,20 aluminium round bar, 40mm square aluminium bar, D16 mild steel round bar	16.98
	Easy Composites Ltd	D10 Roll wrapped carbon fibre tube (0.5m)	12.61
Fasteners/Fixtures	ME Stores	Nuts (M10, M5 LH thread, M5, M6) Various socket head bolts M5x130 Studding	2.50
	RS Components	Ruland Collar (OF-MSP-20-A) (x18) Pillow block bearings (IGUS KSTM12) M5 rod end (POS 5EC L), M5 rod end (POS 5EC)	472.90
Chassis	ME Stores	Aluminium sheets (3mm & 4mm thick) 20mm square steel bar, D20 round steel bar	58.22
	Easy Composites Ltd	CF Foam Core Panel 980x480, 480x480 6mm thick	171.50
Safety Equipment	RS Components	Half mask respirator, gas vapour filter, mist filter, filter retainer	139.90
Total = £1325			

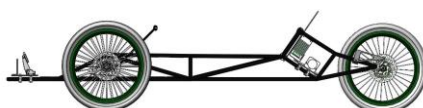


DISCUSSION AND CONCLUSIONS

Potential Component Failure and Mitigation (AWP)

Table 34 - failure modes with corresponding mitigation methods

Failure Mode	Description	Mitigation
Shell interference with new chassis	The new chassis has been designed to fit within the existing shell. However, dimensions of shell CAD model may be slightly different to reality due to old age.	Minor interference can be mitigated by cutting the problematic areas (especially the rim of the shell) manually. In the unlikely event of major interference, carbon fibre wet layup can be used to modify the shape of the shell.
Incompatibility between front brake caliper and front brake caliper mounting arm	Mounting holes are a standard dimension for 'Post-mount' brake calipers. However, caliper body dimensions are brand-specific so there could be interference between the caliper body and the mounting arm designed.	Minor interference can be mitigated by manual filing of the aluminium arm. More severe interference (where filing would compromise the bracket strength) would require a new arm to be manufactured by CNC. Alternatively, use 3D printing with carbon fibre infused filament, similar to that used for the rear caliper arm.
Excessive torsional deflection of steering column	The long and narrow carbon fibre tube used for the steering column may exhibit excessive torsional deflection that can hinder the accuracy of the steering system and reduce driver confidence in the car	Use a carbon fibre tube with a larger diameter to increase its polar moment of area and reduce torsional deflection. This would require a new 3D printed bracket to connect this tube to the handlebars, and an insert to adapt the tube to the current universal joint or purchase a bigger universal joint.
Camber adjustment may change during operation	The camber adjustment relies on the friction between the 'l' bracket and the chassis mounting plates. Vibrations during operation may cause the camber angle to change. Inspection is advised after every run.	Apply high-friction shims between 'L' bracket and chassis mounting plates. Anti-vibration pads could also be used to increase friction as well as damping. Effect of vibrations could be mitigated further by using nyloc nuts and anti-vibration washers.
Tie-rod and drag-link insert bonding failure	Aluminium inserts were bonded at each end of the carbon fibre tie-rod and drag-link tubes. Bonding strength depends on many external factors (e.g. temperature and humidity) so there is a possibility of these bonds failing.	Drill a small M2 hole through the carbon fibre tubes and aluminium inserts and connect the two using a spring pin. Alternatively, if this results in cracking of the tubes, replacement solid aluminium rods should be made with the threads tapped out at each end to be used as a last-resort (albeit heavier) replacement.
M5 rod-end failure in 'L' Bracket subassembly	The low static and dynamic loads allowed the rod-ends to be loaded in bending without any observable deflection. However, this could be a potential source of failure.	Replace M5 components with similar M6 variants, if necessary. Purchase M6 rod-ends, M6 threaded rod for the kingpin axis, M6 nuts and manufacture kingpin axis spacers, all to be used as potential spares. If needed, the M5 holes in the angled brackets and 'L' brackets can be drilled out to M6 and re-tapped where necessary by hand at the competition.
M5 bolt failure in the axle mount component	The shock loads and lateral loads translated to the axle mount component from the wheel may	Replace M5 bolt with an M6 bolt. If necessary, the axle mount component can be inspected and measure in its angular misalignment mitigation position and an equivalent continuous, single part



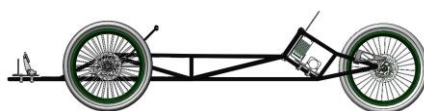
	cause this bolt to fail due to high shear stresses.	can be manufactures using CNC to replace the two-part component.
Failure of one or more cured joints of the spaceframe	When repeatedly loaded with a drivers weight, used for extended use outdoors, or exposed to hot road temperatures, the wrapped carbon fibre joints may weaken and deflect.	All cured joints of the spaceframe are inspected regularly and physically tested using weight. A record of chassis deflections should be kept to identify when a joint could become worn. In this case, reapply the layup process with more layers to create a new undamaged structure, re-test before use.
Insufficient visibility for driver	When designing the chassis, a 5' 5" human model was used to confirm that the vision of the driver was not affected in any way. If the driver, when suited up to race, exceeds the size of the model, her vision may be blocked.	If the driver's vision is blocked in any way, a wet layup process can be used to alter the shell in order to ensure full visibility is restored. Positions of windows on the shell may also be altered if necessary.

Conclusions

The overall objectives for the project were as follows:

1. Design a chassis that will comfortably fit an average female driver, provide mounting points for all components and be mounted to the existing aerodynamic shell with minimal modifications.
2. Design a steering system which maximises efficiency and provides an adequate level of feedback to the driver, allowing for adjustments to be made to the front wheel alignment.
3. Implement a powertrain interface on the developed chassis that will be compatible with the developments of Powertrain DMT Group 27.

The final chassis successfully fit an average female driver, provided mounting points for all components and achieved a weight reduction of 23% compared to last years' entry with all components attached. Though the powertrain system had not yet been produced by the Powertrain DMT team at the time of the project ending, the chassis interface was fully compatible with its design. While thorough testing did not occur due to the reduced timeline of the project, the validity of the final product in meeting loading conditions and achieving a high efficiency was backed by in-depth stress and deflection analysis and steering system design calculations. Additionally, the steering system incorporated adjustable front wheel alignment, allowing the efficiency of the system to be maximised regardless of the driver. Although the project was expected to consume most of the budget for the entire vehicle, significantly less than half of the budget was used at £1325. This project, in conjunction with the work produced by the Powertrain Team, will put the SEM team for the following year in a very good position to have a completed vehicle, ready to compete in the race.



INDIVIDUAL CRITIQUES

Jessica Eichel

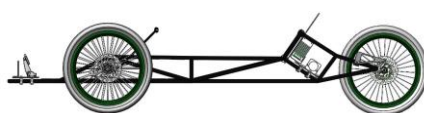
Overall, it has been a pleasure working together with this highly motivated and talented team to exceed our project aims and objectives. The team's approach of emphasising simple engineering evaluations and calculations to inform practical decisions on manufacturing proved successful and allowed completion of the entire SEM chassis and steering system on time and before the lockdown was implemented. The project management approach worked particularly well, whereby one member ensured the Gantt chart remained up to date and each member was formally assigned weekly tasks on Microsoft teams.

My main roles within the team were contributing to the design development of the chassis including materials selection and manufacturing methods as well as prototyping and testing of the spaceframe design and layup. I was also responsible for the procurement and budgeting, providing a valuable part in ensuring all deliverables were met on time. Being part of a larger SEM team provided a wider insight from our supervisor in weekly meetings, as well as the Team Principal, the Powertrain Team, and the formula student team. The main improvements, preventing the SEM vehicle from being fully finished, was a lack of collaboration early on with the Powertrain Team and the Team Principal, projects in future years should aim to improve this relationship.

Carlos Firgau

Initially, this project seemed very ambitious due to its wide scope, although I particularly liked being able to develop unique ideas in different areas of the vehicle. At first, we did not have the independence that we had expected – many of the decisions needed to be confirmed by the Shell Eco-marathon team principal and chiefs. This was different from other DMT groups but it ultimately had a positive effect on our learning experience, being more representative of a real-world engineering environment. This was especially true as we often had to rely on information provided by the Powertrain DMT to be able to proceed in our own design. More frequent meetings would have been beneficial and are an area of improvement for future projects.

I particularly enjoyed the position of Team Lead where I could make the operational decisions that shaped our final design, relying on the essential knowledge and contributions from the rest of my team. This project allowed me to delve deeper into areas of my own interest in automotive design such as vehicle dynamics and steering characteristics, and to increase my knowledge of the behaviour of carbon fibre. Ultimately, I believe that my methodical approach and attention to detail contributed positively to the robustness of the carbon fibre chassis and the effectiveness of the steering system.



Asad Raja

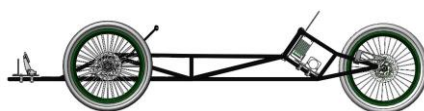
Despite the project being cut short, the team was able to produce the chassis and steering in its essentially complete form and conduct some product testing. This is a mark of the team's consistently proactive working. An early parameter of efficient working that was set by the Project Supervisor was completing the design phase of the project in first term, having the formal Design Review before the holidays, which was achieved. As the Team Secretary, I was responsible for the project structure, producing a detailed Gantt chart with sufficient contingency and holding meetings at least once a week to evaluate progress and make action plans. This effective project planning, which was one of the strengths of the project, meant that internal and external deadlines were met. A dedication to Shell Eco-marathon beyond the DMT project, innovation and thorough analysis and the agreeable nature of all team members to foster a positive dynamic were other integral strengths.

The main weakness of the project was occasional ineffective communication or unequal distribution of workload. Team members would sometimes be modest or selective when updating the team on their contributions. This would lead to a lack of clarity on the process that was taken to come upon certain decisions or the progress of overall tasks. Though occasional more formal and thorough reviews would reveal the true amount and distribution of work, which the project process would then be retrospectively adapted to, a more honest and open approach could have been taken throughout.

Rahman Al-Shabazz

Prior to starting, I had my concerns on the challenges we would experience over the course of the project given its large scope. However, I was fortunate in being able to work alongside intellectual and driven individuals and am proud of the final result. This has been the best organised group I have worked with over the course of my academic career, and I believe this played a big part in our success. Weekly, in-person meeting where actions tasks were set and the effective use of the OneDrive system to collect all our work, ensured the team made consistent and efficient progress. The main area for improvement would be the communication with the Powertrain Team. We failed to set robust deadlines for certain designs which meant our team would occasionally be waiting for dimensions or other information before we could proceed with our work.

My main role in the team was the overall development of spaceframe structure using CAD. As well as conducting my own research and developing ideas, this required that I communicated constantly with all members to ensure their respective contributions to the chassis' design did not interfere with each other. As well as this, I was responsible for exploring the risks involved when working with carbon fibre and constructed the risk assessments needed before manufacture could begin – amongst other smaller tasks. Overall, I feel we worked very well together and am pleased with the final product.



REFERENCES

- Al-Shabazz, R., Eichel, J., Firgau, C. & Raja A. (2020a) *Project Quality Plan*. 2nd Edition. London, United Kingdom: Imperial College London.
- Al-Shabazz, R., Eichel, J., Firgau, C. & Raja A. (2020b) *Progress Report*. 1st Edition. London, United Kingdom: Imperial College London.
- Avid (2012) *OEM Product Technical Specifications*. Available from: http://www.dirtfreak.co.jp/cycle/sram/service/avid/avid_technical_specifications_my13_updates.pdf
- Childs, P. (2019) *Mechanical Design Engineering Handbook*. 2nd Edition. United Kingdom: Elsevier.
- Easy Composites Ltd (2019) *Roll Wrapped Carbon Fibre Tube*. Mechanical Properties and Specification. Available from: <https://www.easycomposites.co.uk/#!/cured-carbon-fibre-products/carbon-fibre-tube/roll-wrapped-carbon-fibre-tube/carbon-fibre-tube-roll-wrapped-8mm.html>
- Fastenal (2009) *Fastenal Engineering & Design Support. Bolted Joint Design*. Winona, Minnesota, United States of America.
- Fastener Mart (2015) *Metric Bolts, Screws & Nuts Tightening Torques*. Available from: https://www.fastenermart.com/files/metric_tighten_torques.pdf
- Fekete, J.R. (2017) *Carbon Fibre Reinforced Polymer. Automotive Steels*. Available from: <https://www.sciencedirect.com/topics/engineering/carbon-fibre-reinforced-polymer/pdf>
- Grabarczyk, M. (2003) *Center of body mass and the evolution of female body shape*. American Journal for Human Biology. p.144-150 Volume 15 Issue 2.
- Grampian Fasteners (2017) *Torque Settings*. Available from: https://www.grampianfasteners.com/files/95b2c19b-1d29-4624-abdf-0813df2db3ac/Torque_Settings.pdf
- Guinness World Records (2018) *Most fuel-efficient vehicle (prototype)*. Available from: https://www.guinnessworldrecords.com/world-records/most-fuel-efficient-vehicle?fb_comment_id=874403022578406_1981249211893776
- King, J.E. (1989) *Failure in composite materials*. Metals and Materials 5. Available from: http://publications.aston.ac.uk/id/eprint/23791/1/Failure_in_composite_materials.pdf
- Kovacevic, S., Vučinić, J., Kirin, S. & Pejnović, N. (2010) *Impact of anthropometric measurements on ergonomic driver posture and safety*. Periodicum Biologorum.
- Lin, W. & Yoda, T. (2017) *Classifications, Design Loading, and Analysis Methods*. Bridge Engineering. p.1-30.
- Merlin Cycles (2014) *Buyers guide to suspension forks*. Available from: <https://www.merlincycles.com/blog/buyers-guide-to-suspension-forks/>
- Milliken, W. & Milliken, D. (1995) *Race Car Vehicle Dynamics*. 5th Edition. Warrendale, Pennsylvania, United States of America: Society of Automotive Engineers, Inc.
- Occupational Health & Safety (2009) *Carbon fibre composites – OHS information sheet*. Melbourne, Australia: Monash University. Available from: <https://www.monash.edu/ohs/info-docs/safety-topics/chemical-management/carbon-fibre-composites-ohs-information-sheet>
- Riley, W. & George, A. (2002) *Design, Analysis and Testing of Formula SAE Chassis*. Ithaca, New York, United States of America: Cornell University.
- Santing, J., Onder, C., Bernard, J., Isler, D., Kobler, P., Kolb, F., Weidmann, N. & Guzzella, L. (2007) *World's Most Fuel Efficient Vehicle. Design and Development of PAC CAR II*. Zurich, Switzerland: vdf Hochschulverlag AG.
- Seward, D. (2014) *Race Car Design*. 1st Edition. United Kingdom: Palgrave.
- Shell Eco-marathon. (2020) *Shell Eco-marathon 2020 Programme Update*. Available from: <https://www.shell.com/make-the-future/shell-ecomarathon/for-participants/2020-programme-update.html>
- Singh, R. (2010) *Structural Performance Analysis of Formula SAE Car*. Patiala, Punjab, India: Chitkara Institute of Engineering and Technology
- Simmons, S. (2019) *2020 Official Rules. Chapter 1*. Shell Eco-Marathon.
- Steinberg, D. (2000) *Vibration Analysis for Electronic Equipment*. 3rd Edition. New York, United States of America: Wiley.
- Waterman, B. (2011) *Design and Construction of a Space-frame Chassis*. Perth, Australia: University of Western Australia
- William Tools Co. (2019) *Standard Bolt Tightening Torque*. Available from: <https://www.wtools.com.tw/STANDARD-BOLT-TIGHTENING-TORQUE.shtml>

